

Soft-Radial Projection for Constrained End-to-End Learning

Philipp J. Schneider Daniel Kuhn

Risk Analytics and Optimization Chair, EPFL

{philipp.schneider, daniel.kuhn}@epfl.ch

February 4, 2026

Abstract

Integrating hard constraints into deep learning is essential for safety-critical systems. Yet existing constructive layers that project predictions onto constraint boundaries face a fundamental bottleneck: *gradient saturation*. By collapsing exterior points onto lower-dimensional surfaces, standard orthogonal projections induce rank-deficient Jacobians, which nullify gradients orthogonal to active constraints and hinder optimization. We introduce *Soft-Radial Projection*, a differentiable reparameterization layer that circumvents this issue through a radial mapping from Euclidean space into the *interior* of the feasible set. This construction guarantees strict feasibility while preserving a full-rank Jacobian almost everywhere, thereby preventing the optimization stalls typical of boundary-based methods. We theoretically prove that the architecture retains the universal approximation property and empirically show improved convergence behavior and solution quality over state-of-the-art optimization- and projection-based baselines.

1 Introduction

Many decision-making systems operate under hard constraints during both training and deployment—for example, safety envelopes in autonomous driving, actuator limits in robotics (Brunke et al., 2022), or budget and capacity constraints in operations. While neural networks are powerful function approximators, they are not inherently constraint-aware, and naive usage can lead to *infeasible* outputs precisely in scenarios where constraint violations have serious consequences. We formalize constrained learning objectives and propose architectural mechanisms that enforce feasibility *by construction*.

Setup. Let $\mathcal{Z} \subseteq \mathbb{R}^d$ be the input space, $\mathcal{Y} \subseteq \mathbb{R}^n$ the target space, and $\mathcal{C} \subseteq \mathbb{R}^n$ the feasible set of decisions, assumed closed and convex with a nonempty interior. This assumption is without loss of generality, as we can always restrict the ambient space to the affine hull of the convex set. Data are drawn from a distribution \mathbb{P} on $\mathcal{Z} \times \mathcal{Y}$ with marginal \mathbb{P}_Z on \mathcal{Z} . We define the policy space Π as the set of all measurable mappings $\pi : \mathcal{Z} \rightarrow \mathbb{R}^n$ that map an input z to a decision.

Supervised learning. Let $(z, y) \sim \mathbb{P}$. We learn an optimal policy by solving

$$\begin{aligned} \min_{\pi \in \Pi} \quad & \mathbb{E}_{(z,y) \sim \mathbb{P}} [\ell(\pi(z), y)] \\ \text{s.t.} \quad & \pi(z) \in \mathcal{C} \quad \text{for } \mathbb{P}_Z\text{-a.e. } z, \end{aligned} \tag{1}$$

where $\ell : \mathcal{C} \times \mathcal{Y} \rightarrow \mathbb{R}$ is a chosen loss. This formulation covers standard regression tasks as well as imitation learning, where the label y represents a hindsight-optimal decision $\pi^*(z)$. In such cases, ℓ quantifies the distance to the optimal decision or a regret surrogate.

Task-driven learning. Without labels, we measure performance directly via a task cost $c : \mathcal{Z} \times \mathcal{C} \rightarrow \mathbb{R}$ and optimize

$$\begin{aligned} \min_{\pi \in \Pi} \quad & \mathbb{E}_{z \sim \mathbb{P}_Z} [c(z, \pi(z))] \\ \text{s.t.} \quad & \pi(z) \in \mathcal{C} \quad \text{for } \mathbb{P}_Z\text{-a.e. } z. \end{aligned} \tag{2}$$

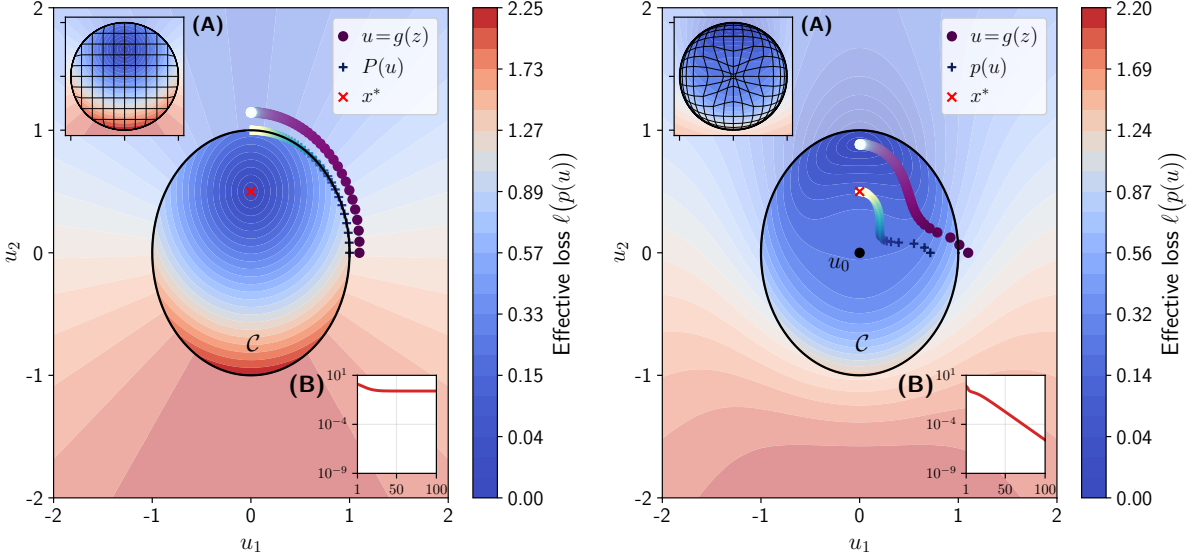
This formulation aligns the training objective with the downstream operational cost, thereby circumventing the potential objective mismatch inherent in surrogate supervised targets (Donti et al., 2017; Elmachtoub & Grigas, 2022; Rychener et al., 2023; Chenreddy & Delage, 2024).

Feasibility by construction. Optimization over the space of constrained functions is generally intractable. However, we can simplify the problem by leveraging the *Interchangeability Principle* (Rockafellar & Wets, 2009, Theorem 14.60). Applied to the task-driven formulation (2), this principle establishes that minimizing the expected cost is equivalent to minimizing the cost pointwise for almost every input z , formally $\inf_{\pi \in \Pi, \pi(z) \in \mathcal{C}} \mathbb{E}_{z \sim \mathbb{P}_Z} [c(z, \pi(z))] = \mathbb{E}_{z \sim \mathbb{P}_Z} [\inf_{x \in \mathcal{C}} c(z, x)]$. This equivalence allows us to solve the functional problem by finding a pointwise optimal decision for any given input z . We enforce constraints constructively by reparameterizing the decision policy: we optimize an unconstrained candidate function $g : \mathcal{Z} \rightarrow \mathbb{R}^n$ composed with a fixed projection operator, such that $\pi(z) = \text{Proj}(g(z))$.

The geometric properties of the projection are decisive for the optimization landscape. The standard approach is the *orthogonal projection* of a vector $u \in \mathbb{R}^n$, denoted $P(u) = \arg \min_{v \in \mathcal{C}} \|u - v\|^2$. While P guarantees feasibility, it maps the entire exterior space onto the lower-dimensional boundary $\partial \mathcal{C}$. In Figure 1a, we demonstrate the phenomenon of gradient saturation. This occurs when the unconstrained output $u = g(z)$ falls outside \mathcal{C} and the level sets of the objective are orthogonal to the boundary. Because P collapses the exterior space onto the surface $\partial \mathcal{C}$, infinitesimal variations of u orthogonal to the boundary result in zero change to the output $\pi(z)$. Consequently, gradient components in these directions are nullified, and the optimization dynamics stall or crawl along the boundary. While the projection is idempotent—preserving the landscape for points already in the interior—the optimization landscape for exterior points $u \notin \mathcal{C}$ becomes rank-deficient.

Soft-Radial Projection to the interior. We instantiate the projection layer as a *Soft-Radial Projection* $p : \mathbb{R}^n \rightarrow \text{Int}(\mathcal{C})$ constructed as a radial homeomorphism. Unlike the orthogonal projection, this map keeps every output strictly inside the interior $\text{Int}(\mathcal{C})$, acting as a smooth reparameterization of the feasible set rather than a distance-minimizing operator. By enforcing a diffeomorphic correspondence almost everywhere, we ensure well-conditioned gradients that guide the optimizer efficiently through the feasible region—and asymptotically toward the boundary if necessary—without the saturation artifacts of the orthogonal projection (cf. Figure 1).

Related work. The challenge of obtaining feasibility guarantees for neural networks has attracted broad interest across research domains, ranging from safety-critical control (Garcia & Fernández, 2015) to decision-focused analytics (Kotary et al., 2021). For an extensive review, we refer to Appendix A. Existing methodologies can be broadly categorized into *optimization-based layers* (e.g., Amos & Kolter, 2017; Agrawal et al., 2019; Donti et al., 2021), which operate via implicit differentiation through iterative solvers, and *constructive layers* that enforce feasibility by design via specialized projections (e.g., Konstantinov & Utkin, 2023; Liang et al., 2024). Crucially, the



(a) Orthogonal projection $P(u)$.

(b) Soft-radial projection $p(u)$ into $\text{Int}(\mathcal{C})$.

Figure 1: Impact of projection geometry on optimization. Comparison of (a) Orthogonal and (b) Soft-Radial Projection on a 2D constrained task (target \times). Main plots visualize the trajectory of the *unconstrained candidate* (\circ) versus the *feasible decision* ($+$). Insets show the coordinate grid warping (A) and training loss (B). Note that soft-radial projection prevents gradient saturation by maintaining descent signals for infeasible inputs.

current research frontier has shifted beyond merely guaranteeing constraint satisfaction (Dala et al., 2018) to ensuring smooth optimization landscapes that facilitate superior learning performance.

Contributions. Our main contributions are as follows:

- We introduce *Soft-Radial Projection*, a closed-form layer for convex sets that ensures strict interior feasibility via a radial transformation (differentiable almost everywhere).
- We provide a theoretical analysis of the gradient dynamics, showing that our construction avoids the rank-deficient Jacobian issues inherent to orthogonal projections.
- We prove that the architecture preserves the *Universal Approximation* property (Theorem 4.1) for continuous functions mapping into $\text{Int}(\mathcal{C})$.
- Empirical results demonstrate the effectiveness of our method in end-to-end learning tasks, including portfolio optimization and resource allocation for demand sharing.

We proceed by formally introducing the soft-radial projection mechanism.

Notation. We use $\|u\|$ for the Euclidean norm of vectors and $\|A\|$ for the spectral norm of matrices. For functions $\psi : \mathcal{Z} \rightarrow \mathbb{R}^n$, we denote the uniform norm by $\|\psi\|_\infty := \sup_{z \in \mathcal{Z}} \|\psi(z)\|$. We write $\text{Int}(\mathcal{C})$ and $\partial\mathcal{C}$ for the interior and boundary of the feasible set. The Jacobian of a differentiable map ϕ is denoted by J_ϕ . We reserve u for unconstrained vectors (pre-projection) and use x or $\pi(z)$ for feasible vectors in \mathcal{C} .

2 Soft-Radial Projection Layer

Many models output a raw vector in \mathbb{R}^n that must satisfy hard constraints at inference time—*e.g.*, neural networks and decoders, control policies, differentiable optimization layers, or amortized solvers. We place a *soft-radial projection layer* $p : \mathbb{R}^n \rightarrow \text{Int}(\mathcal{C})$ downstream of such modules so that, regardless of how the raw output is produced (even if infeasible), the final decision lies in the feasible set.

Concretely, we instantiate the unconstrained candidate g as a parameterized map $g_\theta : \mathcal{Z} \rightarrow \mathbb{R}^n$ (*e.g.*, a neural network). Given the raw output $u = g_\theta(z)$, we set the policy as $\pi_\theta = p \circ g_\theta$, which ensures $\pi_\theta(z) \in \text{Int}(\mathcal{C})$ during training and deployment without penalty tuning or post-hoc repair. The learning objectives (1) and (2) are then instantiated by composing with p (*e.g.*, $\ell(\pi_\theta(z), y)$ or $c(z, \pi_\theta(z))$). This composition turns any base predictor into a constraint-satisfying model while keeping gradients usable for end-to-end training. The remainder of this section develops the geometry and regularity of p needed for gradient-based methods. We first formalize the soft-radial projection p and its raywise components. The construction relies on a smooth contraction toward an anchor point, mapping the entire ambient space into the interior of \mathcal{C} while retaining differentiability almost everywhere.

Definition 2.1 (Soft-Radial Projection). Let $\mathcal{C} \subseteq \mathbb{R}^n$ be a closed, convex set with nonempty interior, and fix an anchor point $u_0 \in \text{Int}(\mathcal{C})$. Let $r : \mathbb{R}_+ \rightarrow [0, 1)$ be continuous and strictly increasing with $r(0) > 0$ and $\lim_{\rho \rightarrow \infty} r(\rho) = 1$.

For any $u \in \mathbb{R}^n$, the *soft-radial projection* of u onto \mathcal{C} is

$$p(u) = u_0 + r(\|u - u_0\|^2) (q(u) - u_0),$$

where $q(u)$ denotes the *hard radial projection* of u onto \mathcal{C} ,

$$q(u) = \begin{cases} u, & \text{if } u \in \mathcal{C}, \\ u_0 + \alpha^*(u)(u - u_0), & \text{otherwise.} \end{cases}$$

The scaling factor $\alpha^*(u)$ is defined as

$$\alpha^*(u) = \sup\{\alpha \in [0, 1] : u_0 + \alpha(u - u_0) \in \mathcal{C}\} \in [0, 1].$$

Remark 2.2. The mapping q projects u onto \mathcal{C} along the ray emanating from the anchor u_0 , in contrast to the usual Euclidean (orthogonal) projection. The soft-radial projection p then interpolates between u_0 and $q(u)$, with interpolation factor governed by $r(\|u - u_0\|^2)$ (see Fig. 2). If we drop the strict-interior requirement and allow $r \equiv 1$, then $p(u) = q(u)$ and the soft-radial projection takes the form of the hard radial projection.

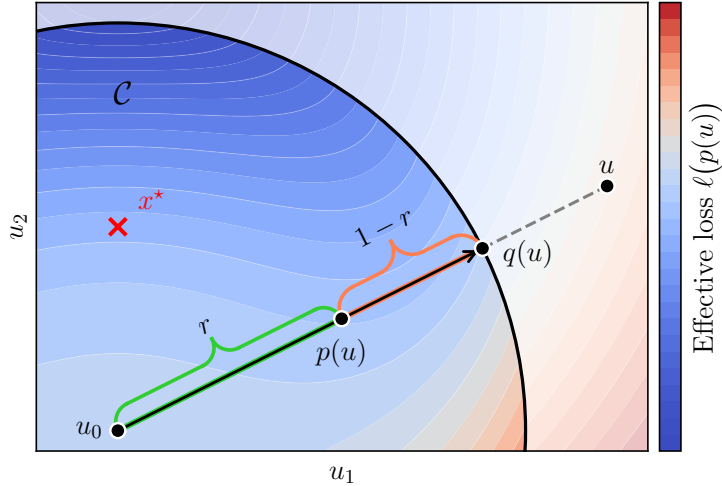


Figure 2: Geometric intuition. A ray from anchor u_0 through input u intersects the boundary $\partial\mathcal{C}$ at the hard radial projection $q(u)$. Our soft-radial mapping $p(u)$ strictly enforces feasibility by smoothly interpolating along the segment $[u_0, q(u)]$ via the radial weight r .

Coordinate convention. The construction of p is invariant under translations of both the input and the set: replacing u by $u - u_0$ and \mathcal{C} by $\mathcal{C} - \{u_0\}$ leaves all statements below unchanged. In the proofs, we therefore assume, without loss of generality, that the anchor is at the origin, $0 \in \text{Int}(\mathcal{C})$, so that $q(u) = u$ for $u \in \mathcal{C}$, $q(u) = \alpha^*(u)u$ otherwise, and the soft-radial projection simply reads $p(u) = r(\|u\|^2)q(u)$. For a general anchor u_0 , one recovers the global form by applying these statements to $\mathcal{C} - \{u_0\}$ and $u - u_0$, and then translating back by u_0 .

Regularity of components. We first record basic properties of the ray map q and the scalar α^* . These facts will be used later to build a raywise parametrization of $\text{Int}(\mathcal{C})$ and to analyze $\ell \circ p$ with first-order methods. In particular, continuity and local Lipschitz continuity of q ensure that composing losses with p preserves standard first-order optimization guarantees on compact sublevel sets.

Lemma 2.3. (Ray intersection and continuity). *Let $\mathcal{C} \subset \mathbb{R}^n$ be nonempty, closed, and convex with nonempty interior, and assume $0 \in \text{Int}(\mathcal{C})$. For any $u \in \mathbb{R}^n$, the set*

$$\{\alpha \in [0, 1] : \alpha u \in \mathcal{C}\}$$

is a nonempty closed interval $[0, \alpha^(u)]$ for a unique $\alpha^*(u) \in [0, 1]$, and $q(u) \in \mathcal{C}$. Moreover, α^* is globally Lipschitz continuous and q is locally Lipschitz (and therefore differentiable almost everywhere by Rademacher's theorem; see, e.g., Federer (1969), Thm. 3.1.6).*

Structural properties of p . We now analyze the global geometry of p . A critical requirement is that p must preserve the *representational capacity* of the model g . Unlike orthogonal projections, which suffer from dimensional collapse by mapping the exterior space onto the boundary surface (a many-to-one mapping), our construction guarantees that p induces a *one-to-one parametrization* of $\text{Int}(\mathcal{C})$ by strictly rescaling radii along rays emanating from the origin.

Assumption 2.4 (Radial monotonicity). The function $r : \mathbb{R}_+ \rightarrow [0, 1]$ is C^1 , strictly increasing with $r'(\rho) > 0$ for all $\rho > 0$, and satisfies $r(0) > 0$ and $\lim_{\rho \rightarrow \infty} r(\rho) = 1$.

Assumption 2.4 ensures that the soft-radial projection is strictly monotonic along rays, providing the topological foundation for the one-to-one mapping. This prevents distinct points on the same ray from collapsing to the same interior location. Specifically, the scalar map $t \mapsto r(t^2)t$ has derivative $\frac{d}{dt}[r(t^2)t] = r(t^2) + 2t^2r'(t^2)$. Since r and r' are positive, this derivative is strictly positive for all $t \geq 0$, confirming that p is an injective transformation into $\text{Int}(\mathcal{C})$.

The mapping p admits a radial decomposition into angular and radial components, simplifying the analysis. Since the projection preserves the direction of the ray \mathbb{R}_+v (the angular component), its behavior is fully characterized by its action on the scalar distance from the origin—the radial component.

Definition 2.5 (Boundary distance). Fix a unit direction $v \in \mathbb{R}^n$ ($\|v\| = 1$). We define the *boundary distance* $\bar{t}(v) \in (0, \infty]$ as the distance from the origin to the boundary of \mathcal{C} along v , given by $\bar{t}(v) := \sup\{t \geq 0 : tv \in \mathcal{C}\}$.

With the boundary established, the radial profile of the projection is defined by the function ψ_v . This map distinguishes between the interior regime, where the ray remains within \mathcal{C} , and the exterior regime, where the input is scaled relative to the boundary.

Definition 2.6 (Scalar projection map). For a fixed unit direction v , define the map $\psi_v : [0, \infty) \rightarrow [0, \infty)$ by $\psi_v(t) := r(t^2) \min\{t, \bar{t}(v)\}$.

By construction, the soft-radial projection satisfies $p(tv) = \psi_v(t)v$. With this decomposition, we now establish the regularity of these components. The following lemma verifies that the boundary distance varies continuously with direction and that the scalar projection is strictly monotonic—properties that are essential for proving the soft-radial projection is a global bijection.

Lemma 2.7. (Regularity of components). *The boundary distance map \bar{t} is continuous on the unit sphere $\{v : \|v\| = 1\}$ (with values in $(0, \infty]$). Moreover, under Assumption 2.4, for any unit direction v , the scalar map ψ_v is continuous and strictly increasing, and its range is exactly $[0, \bar{t}(v))$.*

The raywise analysis in Lemma 2.7 provides the sufficient conditions to characterize the global topology of p . We now formally state the main result: p is a homeomorphism, acting as a reversible deformation of the entire ambient space \mathbb{R}^n onto the feasible interior $\text{Int}(\mathcal{C})$.

Theorem 2.8. (Homeomorphism). *Under Assumption 2.4, the soft-radial projection $p : \mathbb{R}^n \rightarrow \text{Int}(\mathcal{C})$ is a homeomorphism.*

This theorem confirms that the soft-radial layer preserves the topological structure of the unconstrained function space. Avoiding the dimensional collapse of hard projections, p maintains a full-dimensional, bijective correspondence between the parameter space and the feasible policy space.

Differential regularity. Finally, to enable gradient-based learning, we require the projection to be differentiable and the resulting optimization landscape to be free of projection-induced vanishing gradients.

Theorem 2.9. (Differentiability and invertibility). *Under Assumption 2.4, the soft-radial projection p is differentiable almost everywhere on \mathbb{R}^n . The Jacobian $J_p(u)$ is invertible at every point u where it exists.*

The global invertibility of J_p ensures that the mapping is *full-rank* almost everywhere. Consequently, the gradient signal is preserved even when the raw output is far outside \mathcal{C} , strictly avoiding the rank-deficiency and optimization stalling characteristic of standard orthogonal projections.

3 Optimization Guarantees

After establishing the geometry of the projection layer, we now analyze its implications for *unconstrained optimization*. Consider a standard constrained task where we seek to minimize a loss $\ell(x)$ over the feasible set \mathcal{C} . By equipping the model with the soft-radial projection, we transform this into the unconstrained minimization of the *composite objective* $f(u) := \ell(p(u))$, where $u \in \mathbb{R}^n$ denotes the unconstrained candidate vector (*e.g.*, the model output $u = g(z)$).

The following discussion translates the geometric properties of p into concrete optimization guarantees for f , proceeding from the consistency of optimal values to algorithmic convergence rates.

Optimal value equivalence. Our primary requirement is that solving the unconstrained formulation $f(u)$ is equivalent to solving the original constrained objective $\ell(x)$. The homeomorphism property of p guarantees that the global minima align, meaning no valid solutions are lost and no spurious solutions are created.

Theorem 3.1. (Equivalence of optimal values). *Let $\ell : \mathcal{C} \rightarrow \mathbb{R}$ be continuous. With $f := \ell \circ p$, we have*

$$\inf_{u \in \mathbb{R}^n} f(u) = \inf_{x \in \text{Int}(\mathcal{C})} \ell(x) = \inf_{x \in \mathcal{C}} \ell(x).$$

Moreover, $\arg \min f \neq \emptyset$ if and only if $\arg \min_{\mathcal{C}} \ell$ intersects $\text{Int}(\mathcal{C})$. In that case, $u^* \in \arg \min f$ if and only if $p(u^*) \in \arg \min_{\mathcal{C}} \ell$.

First-order correspondence. Beyond agreement of optimal values, optimization algorithms require that first-order stationarity of the unconstrained objective $f := \ell \circ p$ be interpretable in terms of first-order conditions for the original constrained problem. Since $p(\mathbb{R}^n) \subset \text{Int}(\mathcal{C})$, the correspondence we establish is necessarily an *interior* one: it relates stationary points of f to points $x \in \text{Int}(\mathcal{C})$ satisfying $\nabla \ell(x) = 0$. Boundary minimizers of ℓ over \mathcal{C} do not necessarily satisfy $\nabla \ell = 0$ and therefore cannot, in general, be characterized by stationarity of f . The next statement formalizes the interior correspondence via the chain rule and the fact that J_p is invertible almost everywhere.

Proposition 3.2. (Correspondence of stationary points). *Assume ℓ is C^1 on $\text{Int}(\mathcal{C})$. Wherever p is differentiable, with $f = \ell \circ p$ we have*

$$\nabla f(u) = J_p(u)^\top \nabla \ell(p(u)).$$

Consequently, at any point u where the Jacobian $J_p(u)$ is invertible—which holds almost everywhere by Theorem 2.9—the stationary conditions are equivalent:

$$\nabla f(u) = 0 \iff \nabla \ell(p(u)) = 0.$$

This implies that the unconstrained optimization landscape of f introduces no spurious stationary points within the interior of \mathcal{C} .

Remark. If a minimizer x^* of ℓ lies on the boundary $\partial\mathcal{C}$ and satisfies $\nabla\ell(x^*) \neq 0$ (as is typical for constrained optima), Proposition 3.2 implies that there is no stationary point u corresponding to x^* . In this case, minimizing sequences for f must diverge, $\|u_k\| \rightarrow \infty$, pushing $p(u_k)$ toward the boundary.

Global optimality for convex losses. When ℓ is convex, any *interior* stationary point is globally optimal. Since $p(\mathbb{R}^n) = \text{Int}(\mathcal{C})$ and Proposition 3.2 shows that, at points where J_p is invertible, stationarity of $f = \ell \circ p$ is equivalent to $\nabla\ell = 0$ at the corresponding interior point, it follows that p does not introduce spurious interior local minima.

Corollary 3.3. (Global optimality of interior stationary points for convex losses). *Assume ℓ is convex and C^1 on $\text{Int}(\mathcal{C})$, and let $f := \ell \circ p$. If u is a local minimizer of f at which p is differentiable, then $p(u)$ is a global minimizer of ℓ over \mathcal{C} .*

Remark (Anchor). At the anchor $u_0 \in \text{Int}(\mathcal{C})$ we have $J_p(u_0) = r(0)I$, hence

$$\nabla(\ell \circ p)(u_0) = J_p(u_0)^\top \nabla\ell(p(u_0)) = r(0) \nabla\ell(u_0).$$

Thus, the condition $r(0) > 0$ (*cf.* Assumption 2.4) prevents the anchor from becoming an artificial stationary point.

On PL-type conditions. Since the non-linearity of the soft-radial projection p induces non-convexity in the composite objective $f = \ell \circ p$, standard global convergence guarantees do not apply directly. A natural question is whether f satisfies the weaker Polyak–Łojasiewicz (PL) inequality, which would suffice to ensure linear convergence rates. However, even when ℓ is well-conditioned on \mathcal{C} , the saturation $r(\rho) \rightarrow 1$ as $\rho \rightarrow \infty$ can create regions where $\|\nabla f\|$ becomes arbitrarily small while the suboptimality $f - f^*$ stays bounded away from 0, ruling out a global PL bound.

Lemma 3.4. (Absence of a global PL inequality in general). *Even if $\mathcal{C} := B_1(0)$, $\ell(x) := \|x\|^2$ and $u_0 := 0$, there exists no function r satisfying Assumption 2.4 such that $f = \ell \circ p$ satisfies a global PL inequality on \mathbb{R}^n .*

Gradient methods under bounded iterates. Although a global PL inequality fails in general (Lemma 3.4), optimization in practice is typically confined to a bounded region, either *by design* (*e.g.*, projected updates, trust regions, gradient clipping/weight decay) or *by stability* of the dynamics. Since the soft-radial projection p depends on the constraint set \mathcal{C} through the radial map q , global smoothness of p (and hence of $f = \ell \circ p$) cannot be taken for granted for arbitrary convex \mathcal{C} . We therefore record standard convergence guarantees under the common assumption that the iterates remain in a bounded region. We consider the minimization of the expected objective $F(\theta) := \mathbb{E}_z[f(g_\theta(z))]$, where $f = \ell \circ p$, and g_θ is the neural network function parametrized by $\theta \in \Theta$.

Proposition 3.5. (Convergence of stochastic gradient descent). *Let $F(\theta) := \mathbb{E}_z[\ell(p(g_\theta(z)))]$ with iterates confined to a compact set $K \subset \mathbb{R}^p$.*

1. **Smooth Regime:** If \mathbb{P} is absolutely continuous, F is continuously differentiable and L -smooth on K . SGD with step size $\eta_t \propto T^{-1/2}$ satisfies:

$$\min_{0 \leq t < T} \mathbb{E}[\|\nabla F(\theta_t)\|^2] = \mathcal{O}(T^{-1/2}).$$

2. **Nonsmooth Regime:** For general distributions or non-smooth losses, F is locally Lipschitz. Stochastic Subgradient Descent with diminishing steps $\eta_t \rightarrow 0$ converges asymptotically to the set of Clarke stationary points:

$$\lim_{T \rightarrow \infty} \mathbb{E} \left[\min_{v \in \partial F(\theta_T)} \|v\| \right] = 0.$$

Regularity and proof intuition. The regularity of the objective $F(\theta)$ depends on the interplay between the data distribution and the composite function comprising the network g_θ , the projection p , and the loss ℓ . We identify the boundary of the feasible set $\partial\mathcal{C}$ (where p exhibits kinks, see Thm. 2.9) and the activation functions within g_θ as the primary sources of non-differentiability. These points constitute lower-dimensional manifolds in the output space. In the *Smooth Regime*, the absolute continuity of \mathbb{P} implies that the pre-activations $g_\theta(z)$ fall on these *kinks* with probability zero. Consequently, the gradient of the expected objective is well-defined almost everywhere, and standard L -smoothness holds on compact sets. In the *Nonsmooth Regime*, we rely on the fact that p is locally Lipschitz. Since the composition of locally Lipschitz functions (p, g_θ, ℓ) preserves this property, the objective admits bounded Clarke subgradients, ensuring the stability of stochastic subgradient updates.

Robustness to degeneracy. A potential concern is the *degenerate* scenario where the network g_θ collapses the data distribution onto the non-differentiable boundary $\partial\mathcal{C}$. In this case, the optimization effectively switches to subgradient descent. Unlike orthogonal projections where gradients may vanish (due to rank deficiency), the soft-radial projection maintains strict feasibility and non-zero subgradients at the boundary, providing valid descent directions to recover from such collapse.

4 Constrained Universal Approximation

We next demonstrate that the soft-radial projection preserves the expressivity of the underlying model. To establish this, let $\mathcal{Z} \subset \mathbb{R}^d$ be a compact input space and consider a class of continuous functions $\mathcal{G} := \{g_\theta : \mathcal{Z} \rightarrow \mathbb{R}^n \mid \theta \in \Theta\}$, such as sufficiently deep and wide neural networks (Cybenko, 1989; Hornik, 1991). We assume \mathcal{G} is a *universal approximator* in the space of continuous functions $C(\mathcal{Z}, \mathbb{R}^n)$; that is, for any continuous function $\phi \in C(\mathcal{Z}, \mathbb{R}^n)$ and $\delta > 0$, there exists a function $g \in \mathcal{G}$ such that

$$\sup_{z \in \mathcal{Z}} \|g(z) - \phi(z)\| \leq \delta.$$

With \mathcal{G} defined, we aim to show that the constrained model class $\{p \circ g \mid g \in \mathcal{G}\}$ is also a universal approximator for targets in \mathcal{C} . A topological nuance here is that p maps strictly into the *open* interior $\text{Int}(\mathcal{C})$. We must therefore prove that this class can approximate any continuous target $h : \mathcal{Z} \rightarrow \mathcal{C}$ arbitrarily well, even when the target's image contains points on the boundary $\partial\mathcal{C}$.

Recall from Theorem 2.8 that the soft-radial projection $p : \mathbb{R}^n \rightarrow \text{Int}(\mathcal{C})$ is a homeomorphism.

Theorem 4.1. (Universal approximation on \mathcal{C}). *Let $\mathcal{Z} \subset \mathbb{R}^d$ be compact and let \mathcal{G} be a universal approximator on \mathcal{Z} . For every continuous function $h : \mathcal{Z} \rightarrow \mathcal{C}$ and every $\varepsilon > 0$, there exists a function $g \in \mathcal{G}$ such that the constrained predictor $p \circ g$ satisfies*

$$\sup_{z \in \mathcal{Z}} \|p(g(z)) - h(z)\| \leq \varepsilon.$$

Proof intuition. The argument proceeds by density and composition. First, the convexity of \mathcal{C} ensures that continuous functions mapping to the interior $\text{Int}(\mathcal{C})$ are dense in the space of all feasible continuous functions $C(\mathcal{Z}, \mathcal{C})$; thus, any target h admits a uniformly close approximation h_ε that remains strictly interior. Second, because p is a homeomorphism from \mathbb{R}^n onto $\text{Int}(\mathcal{C})$, there exists a continuous pre-image $\phi : \mathcal{Z} \rightarrow \mathbb{R}^n$ such that $p \circ \phi = h_\varepsilon$. The result then follows by applying the universal approximation property of \mathcal{G} to approximate this unconstrained function ϕ .

Remark (Unbounded sets \mathcal{C}). The compactness of the input domain \mathcal{Z} is crucial. It ensures that the image $h(\mathcal{Z})$ is bounded even if the feasible set \mathcal{C} itself is unbounded. Consequently, the requisite pre-images in \mathbb{R}^n remain within a compact subset, where the uniform approximation bounds of \mathcal{G} apply.

Approximation stability. Finally, we ensure that the error bounds of the base estimator transfer to the constrained model. Let $K \subset \mathbb{R}^n$ be compact and let L_K be a Lipschitz constant of p on K . For any continuous function $\phi : \mathcal{Z} \rightarrow \mathbb{R}^n$ and any approximator $g \in \mathcal{G}$ satisfying $\phi(\mathcal{Z}) \subset K$ and $g(\mathcal{Z}) \subset K$, we have

$$\sup_{z \in \mathcal{Z}} \|p(g(z)) - p(\phi(z))\| \leq L_K \sup_{z \in \mathcal{Z}} \|g(z) - \phi(z)\|.$$

This follows immediately by applying the Lipschitz bound for p pointwise on K and taking the supremum over $z \in \mathcal{Z}$.

Implication. Composition with p preserves expressivity and transfers uniform approximation guarantees up to a constant factor. Any uniform error bound for the base class \mathcal{G} translates to the constrained class $p \circ \mathcal{G}$, scaled by the Lipschitz constant L_K of the projection.

5 Numerical Experiments

While Section 1 emphasized safety, strict constraints are equally critical in operations where violations are prohibitive. We evaluate our framework on formulation (2) via portfolio optimization and ride-sharing dispatch; see Appendix C for extended experimental details. For our implementation, we treat the projection as a differentiable layer, allowing us to train the model end-to-end by backpropagating gradients directly through the projection operation to the base network g_θ .¹

5.1 Implementation Details

A critical computational advantage of the soft-radial projection is that the ray-boundary intersection scalar, $\alpha^*(u)$, often admits an efficient closed-form solution. This contrasts sharply with standard layers based on orthogonal projection ($\min_{v \in \mathcal{C}} \|u - v\|^2$). For feasible sets formed by intersecting constraints (such as the capped simplex), orthogonal projection requires solving a constrained quadratic program (QP) for every sample in the batch. These QPs typically lack closed-form solutions, necessitating iterative numerical solvers—such as Dykstra’s algorithm for intersections of convex sets (Dykstra, 1983; Boyle & Dykstra, 1986) or ADMM for splitting complex composite constraints (Boyd et al., 2010)—that significantly slow down the forward pass. Our method circumvents this bottleneck by replacing the iterative QP with a direct, vectorized calculation.

Choice of radial contraction r . Recall from Definition 2.1 that the radial contraction r maps the squared distance $\rho := \|u - u_0\|^2$ to a scaling factor in $[0, 1)$. We parameterize this contraction using

¹Code: <https://anonymous.4open.science/r/soft-radial-projection-e2e-icml/>

smooth sigmoidal mappings satisfying Assumption 2.4. Fixing parameters $\varepsilon \in (0, 1)$ and $\lambda > 0$, we consider three families:

$$\text{(Rational)} \quad r(\rho) = \varepsilon + (1 - \varepsilon) \frac{\rho}{\rho + \lambda} \quad (3)$$

$$\text{(Exponential)} \quad r(\rho) = \varepsilon + (1 - \varepsilon) (1 - e^{-\rho/\lambda}) \quad (4)$$

$$\text{(Hyperbolic)} \quad r(\rho) = \varepsilon + (1 - \varepsilon) \tanh(\rho/\lambda) \quad (5)$$

While all three forms guarantee strict interior feasibility, they differ in their asymptotic saturation rate (see Appendix C.1). Note that the term $r(\rho) + 2\rho r'(\rho)$ remains strictly positive bounded away from zero, ensuring the Jacobian is well-conditioned even at the anchor u_0 .

Computing the radial map. The evaluation of $p(u)$ reduces to computing the scalar $\alpha^*(u)$, defined as the distance from the anchor u_0 to the boundary $\partial\mathcal{C}$ along the ray $(u - u_0)$.

Case 1: Polyhedra (Linear constraints). For sets defined by linear inequalities $Ax \leq b$ (e.g., the simplex or capped simplex), the intersection time is computable exactly without iteration. Since u_0 is strictly interior ($b - Au_0 > 0$), the distance to the boundary is the minimum positive intersection time across all hyperplanes:

$$\alpha^*(u) = \min_{i: a_i^\top (u - u_0) > 0} \frac{b_i - a_i^\top u_0}{a_i^\top (u - u_0)}. \quad (6)$$

This operation is $\mathcal{O}(m)$ per sample and is fully parallelizable.

Case 2: Euclidean balls. For spherical constraints $\|x - c\|_2 \leq R$, the scalar $\alpha^*(u)$ is the unique positive root of the quadratic equation $\|(u_0 + t(u - u_0)) - c\|^2 = R^2$, which admits a simple analytic solution.

Case 3: General convex sets. For general convex sets defined by level sets $h(x) \leq 0$, finding α^* is equivalent to finding the root of the scalar function $\phi(t) = h(u_0 + t(u - u_0))$. Since \mathcal{C} is convex, $\phi(t)$ is convex and monotonic along the ray. The root can therefore be found to machine precision efficiently using Newton-Raphson or Bisection methods.

Baselines. To provide insights with different neural network architectures, we consider for $g_\theta(z)$ a multi-layer perceptron (MLP) and a Long Short-Term Memory (LSTM) (Hochreiter & Schmidhuber, 1997) architecture. To benchmark the efficacy of the soft-radial projection, we compare against state-of-the-art constraint enforcement layers ($\text{Proj}(g_\theta(z))$) across three categories:

- *Softmax (Simplex):* For standard simplex constraints, we utilize the ubiquitous Softmax function with temperature scaling τ . While computationally cheap, it does not generalize to arbitrary convex sets.
- *Orthogonal projection:* We compare against the standard Euclidean projection. As discussed in Section 1, this method is idempotent—preserving the landscape for already-feasible points—but suffers from gradient saturation when inputs lie outside \mathcal{C} .
- *Optimization-based layers:* We evaluate against *Deep Constraint Completion and Correction* (DC3) (Donti et al., 2021), which enforces feasibility via gradient-based corrections, and *HardNet* (Min & Azizan, 2024), a recent architecture specialized for affine constraints.²

²App. C.2 describes the implementation of the respective models for the capped simplex.

5.2 Portfolio Optimization

We consider a financial market with N assets over a finite horizon T . Let $(\Omega, \mathcal{F}, \mathbb{P})$ be a probability space equipped with a filtration $(\mathcal{F}_t)_{t \geq 0}$. At each time step t , the agent observes signals z_t —comprising raw returns augmented with rolling volatility and correlation to the market proxy computed over lookback H —and selects a portfolio weight vector $w_t \in \mathcal{C} \subset \mathbb{R}^N$. Between steps $t-1$ and t , price relatives $y_t \in \mathbb{R}_+^N$ induce a passive drift, evolving weights to $w_{t-1}^+ = (\text{diag}(y_t) w_{t-1}) / (y_t^\top w_{t-1})$. The goal is to maximize the Sharpe ratio of the net returns R_t^{net}

$$\begin{aligned} \max_{\theta} \quad & \frac{\mathbb{E}[R_t^{\text{net}}]}{\sqrt{\text{Var}(R_t^{\text{net}})}} \\ \text{s.t.} \quad & R_t^{\text{net}} = w_{t-1}^\top y_t - \frac{\gamma}{2} \|w_t - w_{t-1}^+\|_1, \quad \forall t, \\ & w_t = \text{Proj}_{\mathcal{C}}(g_\theta(z_t)), \quad \forall t. \end{aligned} \tag{7}$$

Here, γ is the transaction cost parameter and the L_1 norm captures the turnover cost. As the L_1 norm is not differentiable at zero, we replace it in the implementation with the Pseudo-Huber loss. We employ the *component-wise capped simplex*, which generalizes the standard simplex by enforcing asset-specific capacities $c \in (N^{-1}, 1]^N$ to control risk concentration $\mathcal{C} = \{w \in \mathbb{R}_+^N \mid \mathbf{1}^\top w = 1, w \leq c\}$.

Results analysis. Table 1 compares the net Sharpe ratio (SR) and turnover costs utilizing an LSTM architecture within an end-to-end learning framework across different constraint enforcement methods. On the standard simplex (Δ), the soft-radial projection demonstrates superior stability, achieving a Sharpe ratio of $0.90 (\pm 0.03)$ and significantly outperforming Softmax (0.63). Notably, the standard orthogonal Projection fails to converge to a profitable strategy (0.25), yielding high turnover (0.48). This suggests that the LSTM struggles to backpropagate effective gradients through the hard projection step, likely due to vanishing gradients at the constraint boundaries. On the capped simplex (\mathcal{C}), baseline methods (O-Proj, DC3, HardNet) cluster around a Sharpe ratio of 0.62–0.64 with higher variance, while the soft-radial projection maintains its performance (0.90) with minimal turnover (0.05). The reduced standard deviation (± 0.02) indicates that our method is not only more performant but also significantly more robust to initialization than competitive differentiable optimization layers.

Table 1: Portfolio results for *Liquid* dataset, aggregated over five seeds (mean \pm std) with $N = 50$ assets, per-asset capacity $c = 0.05$, and transaction cost $\gamma = 0.1$; see App. C.4.

Feasible Set	Method	SR (Net)	Turnover
Δ	Softmax	0.63 (± 0.19)	0.22 (± 0.05)
	O-Proj	0.25 (± 0.18)	0.48 (± 0.02)
	Soft-Radial	0.90 (± 0.03)	0.06 (± 0.00)
\mathcal{C}	O-Proj	0.64 (± 0.09)	0.22 (± 0.01)
	DC3	0.63 (± 0.08)	0.23 (± 0.01)
	HardNet	0.62 (± 0.11)	0.19 (± 0.01)
	Soft-Radial	0.90 (± 0.02)	0.05 (± 0.00)

5.3 Ride-Sharing Dispatch

To demonstrate generalizability, we apply our framework to ride-sharing dispatch with a *time-varying budget*. Unlike the fixed portfolio sum, the available fleet size $S_t \in \mathbb{N}_+$ fluctuates over time, causing the feasible set \mathcal{C}_t to expand and contract. In practice, such constraints enforce per-zone capacity limits (*e.g.*, congestion or emissions control) Alonso-Mora et al. (2017); Zardini et al. (2022). At each time step t , the agent observes a demand history window z_t (augmented with sine/cosine encodings for day and week) and a current supply proxy S_t . We seek an allocation $a_t \in \mathbb{R}_+^N$ over N zones to maximize the *served rate* for the upcoming interval. We optimize the empirical average:

$$\begin{aligned} \max_{\theta} \quad & \frac{1}{T} \sum_{t=1}^T \left[\frac{\sum_{i=1}^N \min_{\tau}(a_{i,t}, d_{i,t})}{\sum_{i=1}^N d_{i,t}} \right] \\ \text{s.t.} \quad & a_t = \text{Proj}_{\mathcal{C}_t}(g_{\theta}(z_t)), \quad \forall t, \end{aligned} \quad (8)$$

where d_t is the realized demand in the interval following the observation window. We replace the hard minimum with the smooth SoftMin, $\min_{\tau}(x, y) = -\tau \log(e^{-x/\tau} + e^{-y/\tau})$, to maintain non-zero gradients even when supply exceeds demand ($a_{i,t} > d_{i,t}$). The constraint set is a scaled capped simplex $\mathcal{C}_t = \{a \in \mathbb{R}_+^N \mid \mathbf{1}^\top a = S_t, a \leq \kappa S_t\}$. We implement Proj via a *scaling transformation* (homothety): the network output is normalized by S_t , projected onto the canonical unit capped simplex, and subsequently rescaled by S_t . This effectively maps the dynamic constraint geometry to a fixed reference polytope.

Table 2: Ride-sharing dispatch results, aggregated over five random seeds (mean \pm std), for the top $N = 150$ activity zones and zone capacity $\kappa = 0.1$; see App. C.5.

Feasible Set	Method	Served Rate
\mathcal{C}_t	Softmax	0.84 (± 0.00)
	O-Proj	0.70 (± 0.01)
	DC3	0.84 (± 0.00)
	HardNet	0.84 (± 0.00)
	Soft-Radial	0.84 (± 0.00)

Results analysis. Table 2 summarizes the served rate (demand fulfillment) using an MLP policy. Unlike the stochastic portfolio domain, the ride-sharing environment exhibits stable gradient signals, allowing the unconstrained Softmax baseline to reach a high served rate of 0.84. In the constrained setting (\mathcal{C}_t), we observe a performance saturation: DC3, HardNet, and our proposed soft-radial projection converge to the same solution quality (0.84 ± 0.00). This confirms that the soft-radial projection effectively recovers the optimal feasible policy, matching the performance of specialized differentiable optimization layers. Conversely, the standard orthogonal projection significantly underperforms (0.70), again highlighting the detrimental effect of hard boundary constraints on gradient flow during training.

6 Conclusion

This paper introduced *soft-radial projection* to address the gradient saturation inherent in orthogonal projection layers. By constructing a radial homeomorphism to the interior of a convex set, we ensure

strict feasibility and model expressivity (Theorem 4.1) without the computational bottleneck of iterative solvers. Empirically, this approach yields superior solution quality compared to optimization-based baselines, effectively balancing theoretical rigor with practical efficiency. These results establish soft-radial projection as a robust, plug-and-play primitive for imposing hard constraints in end-to-end learning.

Limitations. Our framework relies on the convexity of the feasible set to ensure unique radial intersections, preventing immediate application to non-convex manifolds. Additionally, the method requires a known interior anchor point; while straightforward in our tested domains, automating anchor selection for arbitrary high-dimensional sets and analyzing the stability implications of dynamic anchors remain important directions for future work.

References

Agrawal, A., Amos, B., Barratt, S., Boyd, S., Diamond, S., and Kolter, Z. Differentiable convex optimization layers. In *Advances in Neural Information Processing Systems*, pp. 9562–9574. Curran Associates, Inc., 2019.

Alonso-Mora, J., Samaranayake, S., Wallar, A., Frazzoli, E., and Rus, D. On-demand high-capacity ride-sharing via dynamic trip-vehicle assignment. *Proceedings of the National Academy of Sciences*, 114(3):462–467, 2017.

Amos, B. and Kolter, J. Z. Optnet: Differentiable optimization as a layer in neural networks. In *International Conference on Machine Learning*, pp. 136–145. PMLR, 2017.

Boyd, S., Parikh, N., Chu, E., Peleato, B., and Eckstein, J. Distributed optimization and statistical learning via the alternating direction method of multipliers. *Foundations and Trends® in Machine Learning*, 3(1):1–122, 2010.

Boyle, J. P. and Dykstra, R. L. A method for finding projections onto the intersection of convex sets in Hilbert spaces. In Dykstra, R., Robertson, T., and Wright, F. T. (eds.), *Advances in Order Restricted Statistical Inference*, pp. 28–47, New York, NY, 1986. Springer New York.

Brodie, J., Daubechies, I., De Mol, C., Giannone, D., and Loris, I. Sparse and stable Markowitz portfolios. *Proceedings of the National Academy of Sciences*, 106(30):12267–12272, 2009.

Brouwer, L. Über Abbildung von Mannigfaltigkeiten. *Mathematische Annalen*, 71:97–115, 1912.

Brunke, L., Greeff, M., Hall, A. W., Yuan, Z., Zhou, S., Panerati, J., and Schoellig, A. P. Safe learning in robotics: From learning-based control to safe reinforcement learning. *Annual Review of Control, Robotics, and Autonomous Systems*, 5(1):411–444, 2022.

Charbonnier, P., Blanc-Feraud, L., Aubert, G., and Barlaud, M. Two deterministic half-quadratic regularization algorithms for computed imaging. In *International Conference on Image Processing*, volume 2, pp. 168–172, 1994.

Chenreddy, A. R. and Delage, E. End-to-end conditional robust optimization. In *Uncertainty in Artificial Intelligence*, pp. 736–748, 2024.

Constante-Flores, G. E., Chen, H., and Li, C. Enforcing Hard Linear Constraints in Deep Learning Models with Decision Rules. In *Advances in Neural Information Processing Systems*, volume 38. Curran Associates, Inc., 2025.

Cybenko, G. Approximation by superpositions of a sigmoidal function. *Mathematics of Control, Signals and Systems*, 2(4):303–314, 1989.

Dalal, G., Dvijotham, K., Vecerik, M., Hester, T., Paduraru, C., and Tassa, Y. Safe exploration in continuous action spaces. *arXiv preprint arXiv:1801.08757*, 2018.

Davis, D., Drusvyatskiy, D., Kakade, S., and Lee, J. D. Stochastic subgradient method converges on tame functions. *Foundations of Computational Mathematics*, 20(1):119–154, 2020.

Davis, M. H. and Norman, A. R. Portfolio selection with transaction costs. *Mathematics of Operations Research*, 15(4):676–713, 1990.

Deng, K., Zhang, H., Lu, J., and Sun, H. HoP: Homeomorphic polar learning for hard constrained optimization. *arXiv preprint arXiv:2502.00304*, 2025.

Donti, P., Amos, B., and Kolter, J. Z. Task-based end-to-end model learning in stochastic optimization. In *Advances in Neural Information Processing Systems*, volume 30, pp. 5490–5500. Curran Associates, Inc., 2017.

Donti, P. L., Rolnick, D., and Kolter, J. Z. DC3: A learning method for optimization with hard constraints. In *International Conference on Learning Representations*, 2021.

Dykstra, R. L. An algorithm for restricted least squares regression. *Journal of the American Statistical Association*, 78(384):837–842, 1983.

Elmachtoub, A. N. and Grigas, P. Smart “predict, then optimize”. *Management Science*, 68(1):9–26, 2022.

Federer, H. *Geometric Measure Theory*, volume 153 of *Grundlehren der mathematischen Wissenschaften*. Springer-Verlag, Berlin, Germany, 1969.

Garcia, J. and Fernández, F. A comprehensive survey on safe reinforcement learning. *Journal of Machine Learning Research*, 16(42):1437–1480, 2015.

Ghadimi, S. and Lan, G. Stochastic first-and zeroth-order methods for nonconvex stochastic programming. *SIAM Journal on Optimization*, 23(4):2341–2368, 2013.

Grontas, P. D., Terpin, A., Balta, E. C., D’Andrea, R., and Lygeros, J. Pinet: Optimizing hard-constrained neural networks with orthogonal projection layers. In *International Conference on Learning Representations*, 2026.

Hochreiter, S. and Schmidhuber, J. Long short-term memory. *Neural Computation*, 9(8):1735–1780, 1997.

Hornik, K. Approximation capabilities of multilayer feedforward networks. *Neural Networks*, 4(2):251–257, 1991.

Konstantinov, A. V. and Utkin, L. V. A new computationally simple approach for implementing neural networks with output hard constraints. In *Doklady Mathematics*, volume 108, pp. S233–S241. Springer, 2023.

Kotary, J., Fioretto, F., Van Hentenryck, P., and Wilder, B. End-to-end constrained optimization learning: A survey. In *International Joint Conference on Artificial Intelligence*, pp. 4475–4482, 2021. Survey Track.

Liang, E., Chen, M., and Low, S. H. Homeomorphic projection to ensure neural-network solution feasibility for constrained optimization. *Journal of Machine Learning Research*, 25(329):1–55, 2024.

Markowitz, H. Portfolio selection. *Journal of Finance*, 7(1):77–91, 1952.

Márquez-Neila, P., Salzmann, M., and Fua, P. Imposing hard constraints on deep networks: Promises and limitations. *arXiv preprint arXiv:1706.02025*, 2017. CVPR 2017 Workshop on Negative Results in Computer Vision.

Michaud, R. O. The Markowitz optimization enigma: Is ‘optimized’ optimal? *Financial Analysts Journal*, 45(1):31–42, 1989.

Min, Y. and Azizan, N. HardNet: Hard-constrained neural networks with universal approximation guarantees. *arXiv preprint arXiv:2410.10807*, 2024.

Rockafellar, R. T. *Convex Analysis*. Princeton University Press, Princeton, NJ, 1970.

Rockafellar, R. T. and Wets, R. J.-B. *Variational Analysis*. Springer, 2009.

Rychener, Y., Kuhn, D., and Sutter, T. End-to-end learning for stochastic optimization: A Bayesian perspective. In *International Conference on Machine Learning*, pp. 29455–29472, 2023.

Tordesillas, J., How, J. P., and Hutter, M. Rayen: Imposition of hard convex constraints on neural networks. *arXiv preprint arXiv:2307.08336*, 2023.

Zardini, G., Lanzetti, N., Pavone, M., and Frazzoli, E. Analysis and control of autonomous mobility-on-demand systems. *Annual Review of Control, Robotics, and Autonomous Systems*, 5(1):633–658, 2022.

Zhang, Z., Zohren, S., and Roberts, S. Deep learning for portfolio optimization. *Journal of Financial Data Science*, 2(4):8–20, 2020.

A Related Work

Enforcing hard constraints in neural networks is a fundamental challenge in safety-critical learning, requiring architectures that guarantee output feasibility without compromising optimization stability. The literature can be categorized by the mechanism of enforcement—ranging from soft relaxations and iterative solvers to rigorous geometric constructions. Table 3 summarizes the properties of representative state-of-the-art approaches.

Broadly, constraint layers are distinguished by their dependency on the input context. *Input-independent constraints* involve a feasible set \mathcal{C} that is fixed across all samples (*e.g.*, static actuator limits or portfolio weights), whereas *input-dependent constraints* involve a dynamic geometry $\mathcal{C}(z)$ conditioned on the input. Our work primarily targets the former, establishing a rigorous geometric framework for fixed convex sets. While strict constraint satisfaction is essential, the quality of the learning signal—specifically the ability of backpropagation to provide informative gradients in high-noise regimes—remains under-explored. Existing approaches prioritize inference speed and feasibility during training and execution. However, the convergence behavior toward the true solution and the ultimate optimality gap are less understood, particularly when the enforcement layer significantly alters the unconstrained network output. While this review is not exhaustive—with ongoing developments ranging from accelerated orthogonal projections Grontas et al. (2026) to the use of decision rules for constraint enforcement Constante-Flores et al. (2025)—different applications and noise profiles often demand alternatives to standard orthogonal projection to maintain superior optimization properties.

Table 3: **Comparison with State-of-the-Art Constraint Layers.** We position Soft-Radial Projection among constructive geometric layers that guarantee feasibility without high-dimensional iterative solvers.

Method	Constraint Scope	Input Dep.	Satisfaction	Computation	Gradient Landscape	Univ. Approx.
Soft-Penalty	Any	Yes	No (Penalty)	Closed-Form	Smooth (infeasible)	Yes
DC3 Donti et al. (2021)	General	Yes	Approx.*	Iterative (GD)	Step-size sensitive	Unknown
RAYEN Tordesillas et al. (2023)	Convex (Lin/QC/SOC/LMI)	Limited	Strict	Closed-Form	Clipped / Flat	Unknown
HardNet-Aff Min & Azizan (2024)	Affine	Yes	Strict	Closed-Form	Saturated (Boundary)	Yes
HP Liang et al. (2024)	Ball-Homeomorphic	Yes	Strict	Bisection	Iterative search	Yes
HoP (Polar) Deng et al. (2025)	Star-Convex	Yes	Strict (Int.)	Closed-Form [†]	Polar stagnation	Unknown
RP Konstantinov & Utkin (2023)	Convex (Lin/Quad)	Limited	Strict (Int.)	Closed-Form	Smooth (Saturating)	Unknown
Soft-Radial (Ours)	Convex	No[‡]	Strict (Int.)	C.-F. / 1D Root	Full-rank Jacobian a.e.	Yes

*Asymptotic (linear constraints); heuristic/approximate otherwise; truncated correction in practice.

[†]HoP requires a per-sample interior anchor and a ray-boundary intersection query.

[‡]Current focus is on fixed sets \mathcal{C} , though formulation supports dynamic anchors.

A.1 Approximation and Optimization Approaches

Soft Penalties and Activations. The most straightforward approach, favored by many industry practitioners, relaxes strict constraints into the training objective. Penalty-based methods augment the loss function with a regularization term proportional to the magnitude of constraint violations Márquez-Neila et al. (2017). While this preserves the smoothness of the optimization landscape, it fundamentally fails to guarantee feasibility during inference, particularly in high-dimensional spaces where the volume of the feasible set relative to the ambient space can become negligible. Similarly, standard activation functions (*e.g.*, Sigmoid, Softmax) offer computationally efficient

bounds for elementary box or simplex constraints but lack the topological expressivity to model complex coupled constraints or polyhedral boundaries.

Differentiable Optimization and Iterative Correction. To ensure strict satisfaction, a second family of methods embeds optimization solvers directly into the network architecture. Differentiable optimization layers, such as OptNet Amos & Kolter (2017) and CVXPYLayers Agrawal et al. (2019), compute the orthogonal projection of a prediction onto \mathcal{C} by solving a convex program during the forward pass. DC3 Donti et al. (2021) instead utilizes a *completion–correction* scheme, where equality constraints are satisfied via variable completion and inequality violations are reduced through iterative gradient-based correction. While mathematically general, these approaches introduce significant computational overhead. Furthermore, backpropagating through these layers typically relies on implicit differentiation, which assumes the inner solver has reached a stationary point. When truncated for real-time efficiency (*e.g.*, fixed-iteration limits), this assumption is violated, leading to conflict-prone gradient updates where the descent direction of the task loss contradicts the incomplete constraint correction.

A.2 Constructive Geometric Layers

To circumvent the computational cost of iterative solvers, recent research focuses on “Feasibility by Construction” via closed-form surjective mappings $\text{Proj} : \mathbb{R}^n \rightarrow \mathcal{C}$. We classify these geometric approaches into three distinct families:

Gauge and Boundary Projections. RAYEN Tordesillas et al. (2023) enforces convex constraints by selecting a fixed interior point and *rescaling* a predicted direction so that the endpoint remains feasible; the mapping is identity when the step stays inside the set, and otherwise returns the first ray–boundary intersection. HardNet-Aff Min & Azizan (2024) targets *input-dependent affine* inequalities via a closed-form pseudoinverse-based correction that clamps violated constraints to their bounds while moving in directions parallel to already-satisfied constraint boundaries. While both layers are computationally efficient, their piecewise ray/clamping structure can suppress learning signals when constraints are active (*e.g.*, RAYEN becomes insensitive to step magnitude after rescaling, and HardNet-Aff can attenuate gradient components in constraint-normal directions). This suppression can bias training toward boundary-feasible outputs and reduce interior exploration.

Topological Diffeomorphisms. To utilize the set’s interior, topological methods reshape the output space. Homeomorphic Projection (HP) Liang et al. (2024) learns a bi-Lipschitz *invertible neural network* (INN) that approximates a minimum-distortion homeomorphism between the constraint set and a unit ball. At inference, HP maps an infeasible prediction into the ball via the INN inverse and then performs a k -step bisection along the ray to the ball center, requiring repeated INN forward evaluations and feasibility checks; the resulting boundary-feasible point trades computation for accuracy through the bisection depth and depends on the learned mapping distortion. Polar coordinate methods like HoP Deng et al. (2025) attempt an analytic solution but introduce polar stagnation, singularities at the origin where angular components are undefined, resulting in numerical instability near the geometric center.

Radial Interior Mappings. Closely related to our work, Konstantinov & Utkin (2023) propose a “ray-projection” layer that constructs feasible points by scaling a direction vector r from an interior anchor. While effective, this requires a specialized architecture that learns separate polar coordinates ($g(r, s)$) rather than a direct map of the ambient Euclidean space. Furthermore, these

constructions typically do not furnish a global bijection between \mathbb{R}^n and $\text{Int}(\mathcal{C})$, potentially resulting in saturating radial behavior due to the choice of bounded scaling functions (*e.g.*, sigmoids).

Our Contribution: Soft-Radial Projection. We propose a drop-in reparameterization layer for fixed closed convex sets with a non-empty interior. Our mapping acts directly on the unconstrained ambient prediction $u \in \mathbb{R}^n$ as a unified radial homeomorphism $\mathbb{R}^n \rightarrow \text{Int}(\mathcal{C})$. For standard convex geometries—such as balls, ellipsoids, and boxes—the mapping admits a closed-form solution. For general convex sets, we utilize an efficient monotonic 1D root-finding procedure. Crucially, we ensure the mapping is differentiable with an invertible Jacobian almost everywhere, preventing the rank-collapse characteristic of boundary projections. This ensures the learning signal remains non-vanishing even for predictions far outside the feasible set, while preserving the Universal Approximation property of the base network (Theorem 4.1).

B Proofs

In the following sections, we provide complete proofs for the theoretical results. To facilitate readability, we restate each claim prior to its proof.

B.1 Proofs of Section 2

We begin by establishing the regularity of the individual projection components.

Lemma 2.3. (Ray intersection and continuity). *Let $\mathcal{C} \subset \mathbb{R}^n$ be nonempty, closed, and convex with nonempty interior, and assume $0 \in \text{Int}(\mathcal{C})$. For any $u \in \mathbb{R}^n$, the set*

$$\{\alpha \in [0, 1] : \alpha u \in \mathcal{C}\}$$

is a nonempty closed interval $[0, \alpha^(u)]$ for a unique $\alpha^*(u) \in [0, 1]$, and $q(u) \in \mathcal{C}$. Moreover, α^* is globally Lipschitz continuous and q is locally Lipschitz (and therefore differentiable almost everywhere by Rademacher’s theorem; see, *e.g.*, Federer (1969), Thm. 3.1.6).*

Proof. Ray feasibility and intersection. Fix $u \in \mathbb{R}^n$ and consider scalars $\alpha \in [0, 1]$ such that $\alpha u \in \mathcal{C}$. The map $\alpha \mapsto \alpha u$ is continuous and \mathcal{C} is closed, so the set of feasible $\alpha \in [0, 1]$ is closed in $[0, 1]$ and nonempty (since $\alpha = 0$ is always feasible). Convexity of \mathcal{C} implies this set is convex in \mathbb{R} , and any nonempty closed convex subset of \mathbb{R} is an interval; hence it is of the form $[0, \alpha^*(u)]$ for a unique $\alpha^*(u) \in [0, 1]$.

Global Lipschitz continuity of α . Let $\gamma_{\mathcal{C}} : \mathbb{R}^n \rightarrow [0, \infty)$ denote the Minkowski functional (gauge) of \mathcal{C} ,

$$\gamma_{\mathcal{C}}(x) := \inf\{t > 0 : x \in t\mathcal{C}\}.$$

Standard properties of the gauge (see, *e.g.*, Rockafellar (1970), Thm. 14.5 and Chap. 13) imply that $\gamma_{\mathcal{C}}$ is sublinear (convex and positively homogeneous) and finite on \mathbb{R}^n when $0 \in \text{Int}(\mathcal{C})$. Because $0 \in \text{Int}(\mathcal{C})$, there exists $\delta > 0$ with $B(0, \delta) \subset \mathcal{C}$, which yields $\gamma_{\mathcal{C}}(x) \leq \|x\|/\delta$ for all x and, by subadditivity of $\gamma_{\mathcal{C}}$,

$$\gamma_{\mathcal{C}}(x) - \gamma_{\mathcal{C}}(y) \leq \gamma_{\mathcal{C}}(x - y) \leq \frac{\|x - y\|}{\delta} \quad \forall x, y \in \mathbb{R}^n,$$

and

$$\gamma_C(y) - \gamma_C(x) \leq \gamma_C(y - x) \leq \frac{\|y - x\|}{\delta} \quad \forall x, y \in \mathbb{R}^n.$$

Taking the maximum of the two inequalities shows

$$|\gamma_C(x) - \gamma_C(y)| \leq \frac{\|x - y\|}{\delta} \quad \forall x, y \in \mathbb{R}^n,$$

so γ_C is Lipschitz with constant $1/\delta$.

For $u \neq 0$, the feasibility of $\alpha u \in \mathcal{C}$ is equivalent to $\alpha \leq 1/\gamma_C(u)$. Therefore, the feasible $\alpha \in [0, 1]$ form the interval $[0, \min\{1, 1/\gamma_C(u)\}]$, implying that $\alpha^*(u) = \min(1, 1/\gamma_C(u))$, for $u \neq 0$, while for $u = 0$ we clearly have $\alpha^*(u) = 1$. Define a helper function $\psi : [0, \infty) \rightarrow (0, 1]$ by $\psi(t) := \min(1, 1/t)$ for $t > 0$ and $\psi(0) := 1$. The function ψ is 1-Lipschitz on $[0, \infty)$, so for all $u, v \in \mathbb{R}^n$,

$$\begin{aligned} |\alpha^*(u) - \alpha^*(v)| &= |\psi(\gamma_C(u)) - \psi(\gamma_C(v))| \\ &\leq |\gamma_C(u) - \gamma_C(v)| \leq \frac{\|u - v\|}{\delta}. \end{aligned}$$

Thus α^* is globally Lipschitz with constant $1/\delta$.

Local Lipschitz continuity of q . We now bound the variation of $q(u) = \alpha^*(u)u$ on bounded sets. Let $R > 0$ and assume $\|v\| \leq R$ and $\|u\| \leq R$. Then

$$\begin{aligned} \|q(u) - q(v)\| &= \|\alpha^*(u)u - \alpha^*(v)v\| \\ &\leq \|\alpha^*(u)(u - v)\| + \|v(\alpha^*(u) - \alpha^*(v))\| \\ &\leq \|u - v\| + \|v\| \cdot |\alpha^*(u) - \alpha^*(v)| \\ &\leq \|u - v\| + \frac{\|v\|}{\delta} \|u - v\| \\ &\leq \left(1 + \frac{R}{\delta}\right) \|u - v\|. \end{aligned}$$

Hence q is $(1 + R/\delta)$ -Lipschitz on the ball $\{u : \|u\| \leq R\}$, which implies that q is locally Lipschitz on \mathbb{R}^n , completing the proof. \square

Next, we analyze the structural properties of the constructed projection map.

Lemma 2.7. (Regularity of components). *The boundary distance map \bar{t} is continuous on the unit sphere $\{v : \|v\| = 1\}$ (with values in $(0, \infty]$). Moreover, under Assumption 2.4, for any unit direction v , the scalar map ψ_v is continuous and strictly increasing, and its range is exactly $[0, \bar{t}(v))$.*

Proof. Continuity of \bar{t} . We relate $\bar{t}(v)$ to the Minkowski functional (gauge) γ_C . By definition, $\bar{t}(v) = 1/\gamma_C(v)$ (with the convention $1/0 = \infty$). Since γ_C is continuous on \mathbb{R}^n (Lemma 2.3) and the inversion map is continuous on $[0, \infty)$ into $(0, \infty]$, the composition $v \mapsto \bar{t}(v)$ is continuous on the unit sphere.

Properties of ψ_v . For $t \leq \bar{t}(v)$, we have $\psi_v(t) = r(t^2)t$. Strict monotonicity on this interval was established immediately following Assumption 2.4. For $t > \bar{t}(v)$ (which implies $\bar{t}(v) < \infty$), we have $\psi_v(t) = r(t^2)\bar{t}(v)$, which is strictly increasing simply because r is increasing. Continuity holds at $t = \bar{t}(v)$ as both expressions coincide. Finally, since $\psi_v(0) = 0$ and $\lim_{t \rightarrow \infty} \psi_v(t) = \bar{t}(v)$, the range is exactly $[0, \bar{t}(v))$. \square

Building on these established properties, we prove that p is indeed a homeomorphism.

Theorem 2.8. (Homeomorphism). *Under Assumption 2.4, the soft-radial projection $p : \mathbb{R}^n \rightarrow \text{Int}(\mathcal{C})$ is a homeomorphism.*

Proof. We first establish that p is a bijection.

Injectivity. Let $u_1, u_2 \in \mathbb{R}^n$ with $p(u_1) = p(u_2)$. Since p preserves directions (i.e., $p(u) \in \mathbb{R}_+u$), u_1 and u_2 must lie on the same ray, so $u_i = t_i v$ for some unit vector v and $t_i \geq 0$. The scalar map ψ_v from Definition 2.6 satisfies $p(t_i v) = \psi_v(t_i) v$. By Lemma 2.7, ψ_v is strictly increasing, so $\psi_v(t_1) = \psi_v(t_2)$ implies $t_1 = t_2$, and hence $u_1 = u_2$.

Surjectivity. Let $x \in \text{Int}(\mathcal{C})$. If $x = 0$, $x = p(0)$. If $x \neq 0$, set $v = x/\|x\|$ and $s = \|x\|$. Since $x \in \text{Int}(\mathcal{C})$, we strictly have $s < \bar{t}(v)$. By Lemma 2.7, the continuous scalar map ψ_v has range $[0, \bar{t}(v))$. By the Intermediate Value Theorem, there exists a unique t such that $\psi_v(t) = s$, yielding $p(tv) = x$. Moreover, p is continuous on \mathbb{R}^n as it is composed of the continuous scaling function r (Assumption 2.4) and the continuous hard radial projection q (Lemma 2.3). Thus, p is a continuous bijection from \mathbb{R}^n onto $\text{Int}(\mathcal{C})$.

Continuity of Inverse. Since p is a continuous injection from \mathbb{R}^n into an open subset \mathbb{R}^n , the Invariance of Domain theorem Brouwer (1912) guarantees that p is an open map. Because p is a continuous bijection that maps open sets to open sets, it is a homeomorphism between \mathbb{R}^n and its image $\text{Int}(\mathcal{C})$. \square

Finally, we analyze the differentiability of p , establishing that it is a diffeomorphism almost everywhere.

Theorem 2.9. (Differentiability and invertibility). *Under Assumption 2.4, the soft-radial projection p is differentiable almost everywhere on \mathbb{R}^n . The Jacobian $J_p(u)$ is invertible at every point u where it exists.*

Proof. By Lemma 2.3, q is locally Lipschitz and therefore differentiable almost everywhere by Rademacher's theorem. Since r is C^1 , the product $p(u) = r(\|u\|^2)q(u)$ shares the same domain of differentiability. Whenever $J_p(u)$ exists, the product rule gives

$$J_p(u) = r(\|u\|^2) J_q(u) + 2r'(\|u\|^2) q(u) u^\top. \quad (9)$$

We analyze the invertibility of this Jacobian in two cases based on the position of u relative to \mathcal{C} . Note that p is generally not differentiable for $u \in \partial\mathcal{C}$ because the map $\alpha^*(u)$ (and thus q) typically exhibits a kink at the boundary where the active regime switches.

Interior points. For $u \in \text{Int}(\mathcal{C})$ we have $q(u) = u$ and $J_q(u) = I$, hence

$$J_p(u) = r(\|u\|^2) I + 2r'(\|u\|^2) uu^\top.$$

For $u \neq 0$, this matrix has eigenvector $u/\|u\|$, with corresponding eigenvalue $r(\|u\|^2) + 2\|u\|^2 r'(\|u\|^2)$ and all vectors orthogonal to u are eigenvectors with eigenvalue $r(\|u\|^2)$. Assumption 2.4 gives $r(\rho) > 0$ and $r(\rho) + 2\rho r'(\rho) > 0$ for all $\rho \geq 0$, so $J_p(u) \succ 0$ is invertible for all $u \in \text{Int}(\mathcal{C}) \setminus \{0\}$. At the origin, q coincides with the identity in a neighborhood of 0 (because $0 \in \text{Int}(\mathcal{C})$), so $J_q(0) = I$ and the rank-one term vanishes, giving $J_p(0) = r(0) I$, which is invertible since $r(0) > 0$.

Exterior points. For points outside the interior ($u \notin \text{Int}(\mathcal{C})$), $q(u)$ lies on the boundary $\partial\mathcal{C}$. Using the gauge $\gamma_{\mathcal{C}}$ of \mathcal{C} (the Minkowski functional), the condition $u \notin \text{Int}(\mathcal{C})$ implies $\gamma_{\mathcal{C}}(u) \geq 1$, and the hard radial projection is given by $q(u) = u/\gamma_{\mathcal{C}}(u)$. Now fix a point u where $\gamma_{\mathcal{C}}$ is differentiable (which holds almost everywhere by standard results on convex functions, see, *e.g.*, Rockafellar (1970), §25). To simplify notation, let $\lambda := \gamma_{\mathcal{C}}(u) \geq 1$. Differentiating $q(u)$ with respect to u yields the Jacobian

$$J_q(u) = \frac{1}{\lambda}I - \frac{1}{\lambda^2}u\nabla\gamma_{\mathcal{C}}(u)^{\top}.$$

We establish that $J_p(u)$ is invertible by showing its kernel is trivial. Let $h \in \mathbb{R}^n$ satisfy $J_p(u)h = 0$. We decompose h with respect to the subspace $W = \{w \in \mathbb{R}^n \mid u^{\top}w = 0\}$. Any h can be uniquely written as $h = h_W + \beta u$, where $h_W \in W$ and $\beta \in \mathbb{R}$.

First, we compute the product of $J_q(u)$ with the radial component. Since $\gamma_{\mathcal{C}}$ is positively homogeneous of degree 1 by definition, Euler's homogeneous function theorem implies $\nabla\gamma_{\mathcal{C}}(u)^{\top}u = \gamma_{\mathcal{C}}(u) = \lambda$. Using this relation, we find

$$J_q(u)u = \frac{1}{\lambda}u - \frac{1}{\lambda^2}u\underbrace{(\nabla\gamma_{\mathcal{C}}(u)^{\top}u)}_{\lambda} = \frac{1}{\lambda}u - \frac{1}{\lambda}u = 0.$$

For the orthogonal component h_W , we have

$$J_q(u)h_W = \frac{1}{\lambda}h_W - \frac{\nabla\gamma_{\mathcal{C}}(u)^{\top}h_W}{\lambda^2}u.$$

Substituting $h = h_W + \beta u$ and the expression for $J_p(u)$ (9) into the condition $J_p(u)h = 0$ yields

$$r(\|u\|^2)J_q(u)h_W + 2\beta\|u\|^2r'(\|u\|^2)q(u) = 0.$$

Substituting the expansion of $J_q(u)h_W$ allows us to group terms proportional to u . The equation becomes

$$\frac{r(\|u\|^2)}{\lambda}h_W + \mu u = 0,$$

where $\mu \in \mathbb{R}$ captures all radial coefficients:

$$\mu = 2\beta\|u\|^2r'(\|u\|^2)\frac{1}{\lambda} - \frac{r(\|u\|^2)\nabla\gamma_{\mathcal{C}}(u)^{\top}h_W}{\lambda^2}.$$

Projecting the vector equation onto the subspace W eliminates μu , yielding

$$\frac{r(\|u\|^2)}{\lambda}h_W = 0.$$

Since $r > 0$ and $\lambda \geq 1$, we must have $h_W = 0$. Consequently, the radial term must also vanish, so $\mu u = 0$, implying $\mu = 0$. With $h_W = 0$, the expression for μ simplifies to

$$2\beta\|u\|^2r'(\|u\|^2)\frac{1}{\lambda} = 0.$$

Assumption 2.4 ensures $r'(\rho) > 0$ for $\rho > 0$, so we must have $\beta = 0$. Thus $h = 0$, proving that $J_p(u)$ is invertible. Combining the results for interior and exterior points, we conclude that p is differentiable almost everywhere and $J_p(u)$ is invertible wherever it exists. \square

B.2 Proofs of Section 3

We begin by establishing the equivalence of the optimal values between the unconstrained composite optimization $f(u)$ and the constrained optimization objective.

Theorem 3.1. (Equivalence of optimal values). *Let $\ell : \mathcal{C} \rightarrow \mathbb{R}$ be continuous. With $f := \ell \circ p$, we have*

$$\inf_{u \in \mathbb{R}^n} f(u) = \inf_{x \in \text{Int}(\mathcal{C})} \ell(x) = \inf_{x \in \mathcal{C}} \ell(x).$$

Moreover, $\arg \min f \neq \emptyset$ if and only if $\arg \min_{\mathcal{C}} \ell$ intersects $\text{Int}(\mathcal{C})$. In that case, $u^* \in \arg \min f$ if and only if $p(u^*) \in \arg \min_{\mathcal{C}} \ell$.

Proof. By bijectivity of $p : \mathbb{R}^n \rightarrow \text{Int}(\mathcal{C})$,

$$\inf_{u \in \mathbb{R}^n} f(u) = \inf_{x \in \text{Int}(\mathcal{C})} \ell(x).$$

Since $u_0 \in \text{Int}(\mathcal{C})$ and \mathcal{C} is convex, for any $x \in \mathcal{C}$ and $\varepsilon \in (0, 1]$, $x_\varepsilon := (1 - \varepsilon)x + \varepsilon u_0 \in \text{Int}(\mathcal{C})$ and $x_\varepsilon \rightarrow x$ as $\varepsilon \downarrow 0$. By continuity, $\ell(x_\varepsilon) \rightarrow \ell(x)$, hence $\inf_{\text{Int}(\mathcal{C})} \ell \leq \ell(x)$ for all $x \in \mathcal{C}$, implying $\inf_{\text{Int}(\mathcal{C})} \ell \leq \inf_{\mathcal{C}} \ell$. Since $\text{Int}(\mathcal{C}) \subseteq \mathcal{C}$, we also have $\inf_{\mathcal{C}} \ell \leq \inf_{\text{Int}(\mathcal{C})} \ell$. Thus the optimal values coincide.

Finally, $\arg \min f \neq \emptyset$ holds iff there exists $x^* \in \text{Int}(\mathcal{C})$ with $\ell(x^*) = \inf_{x \in \mathcal{C}} \ell(x)$, in which case $u^* = p^{-1}(x^*)$ exists and satisfies $u^* \in \arg \min f$. Conversely, if $u^* \in \arg \min f$, then $p(u^*) \in \text{Int}(\mathcal{C})$ satisfies $\ell(p(u^*)) = \inf_{x \in \mathcal{C}} \ell(x)$, i.e., $p(u^*) \in \arg \min_{\mathcal{C}} \ell \cap \text{Int}(\mathcal{C})$. \square

Next, we establish the equivalence of stationary points between the two objectives.

Proposition 3.2. (Correspondence of stationary points). *Assume ℓ is C^1 on $\text{Int}(\mathcal{C})$. Wherever p is differentiable, with $f = \ell \circ p$ we have*

$$\nabla f(u) = J_p(u)^\top \nabla \ell(p(u)).$$

Proof. The gradient identity follows from the chain rule, using that $p(u) \in \text{Int}(\mathcal{C})$ for all u . If $J_p(u)$ is invertible and $\nabla f(u) = J_p(u)^\top \nabla \ell(p(u)) = 0$, then $\nabla \ell(p(u)) = 0$. The converse is immediate. \square

We then extend this analysis to show that local minimizers of the composite objective correspond to global minimizers of the constrained problem.

Corollary 3.3. (Global optimality of interior stationary points for convex losses). *Assume ℓ is convex and C^1 on $\text{Int}(\mathcal{C})$, and let $f := \ell \circ p$. If u is a local minimizer of f at which p is differentiable, then $p(u)$ is a global minimizer of ℓ over \mathcal{C} .*

Proof. Let u be a local minimizer of f at which p is differentiable. Then $J_p(u)$ is invertible by Theorem 2.9, and $\nabla f(u) = 0$. By Proposition 3.2, $\nabla \ell(p(u)) = 0$. Since $p(u) \in \text{Int}(\mathcal{C})$ and ℓ is convex, $\nabla \ell(p(u)) = 0$ implies that $p(u)$ is a global minimizer of ℓ (over \mathbb{R}^n , and therefore also over \mathcal{C}). \square

We now investigate the convergence rate and demonstrate the absence of a global Polyak-Łojasiewicz (PL) condition, which necessitates a more nuanced convergence analysis.

Lemma 3.4. (Absence of a global PL inequality in general). *Even if $\mathcal{C} := B_1(0)$, $\ell(x) := \|x\|^2$ and $u_0 := 0$, there exists no function r satisfying Assumption 2.4 such that $f = \ell \circ p$ satisfies a global PL inequality on \mathbb{R}^n .*

Proof. The unique minimizer of ℓ over \mathcal{C} is $x^* = 0$, and the corresponding optimal value $\ell^* = 0$. Fix a unit vector v and consider $u(t) := tv$ with $t \geq 0$. For $\mathcal{C} = B_1(0)$ the hard radial projection is $q(u) = u$ if $\|u\| \leq 1$ and $q(u) = u/\|u\|$ otherwise; hence for $t \geq 1$ we have $q(u(t)) = v$ and therefore

$$p(u(t)) = r(t^2)v, \quad f(u(t)) = \|p(u(t))\|^2 = r(t^2)^2.$$

Since $r(t^2) \rightarrow 1$ as $t \rightarrow \infty$, we obtain

$$f(u(t)) - f^* = r(t^2)^2 \rightarrow 1 \quad (t \rightarrow \infty),$$

so along this ray the suboptimality converges to a strictly positive constant. Next, compute the gradient for $t > 1$. On $\{\|u\| > 1\}$, the hard radial projection $q(u) = u/\|u\|$ has Jacobian

$$J_q(u) = \frac{1}{\|u\|} \left(I - \frac{uu^\top}{\|u\|^2} \right),$$

so at $u(t) = tv$

$$J_q(u(t)) = \frac{1}{t} \left(I - vv^\top \right).$$

Substituting the expression for the Jacobian $J_p(u)$ given in (9), we obtain for $t > 1$

$$J_p(u(t)) = \frac{r(t^2)}{t} (I - vv^\top) + 2t r'(t^2) vv^\top.$$

By Proposition 3.2, the gradient is given by $\nabla f(u) = J_p(u)^\top \nabla \ell(p(u))$. Since $\ell(x) = \|x\|^2$ implies $\nabla \ell(x) = 2x$, and specifically $p(u(t)) = r(t^2)v$, we obtain

$$\nabla f(u(t)) = J_p(u(t))^\top (2r(t^2)v) = 2r(t^2) J_p(u(t))v,$$

where the last equality follows from the symmetry of $J_p(u(t))$. When applying the Jacobian matrix to the vector v , the tangential term vanishes because $(I - vv^\top)v = 0$. Only the radial term remains

$$J_p(u(t))v = (2tr'(t^2)vv^\top)v = 2tr'(t^2)v.$$

Substituting this back yields the final gradient norm

$$\|\nabla f(u(t))\| = \|2r(t^2) \cdot 2tr'(t^2)v\| = 4tr(t^2)r'(t^2).$$

It remains to show the existence of a sequence $t_k \rightarrow \infty$ such that $t_k r'(t_k^2) \rightarrow 0$. Since $\lim_{\rho \rightarrow \infty} r(\rho) = 1$, we have $\int_0^\infty r'(\rho) d\rho = 1 - r(0) < \infty$. We claim there exists a sequence $\rho_k \rightarrow \infty$ such that $\sqrt{\rho_k} r'(\rho_k) \rightarrow 0$. Indeed, if not, then there exist $\varepsilon > 0$ and $\rho_0 \geq 0$ such that $\sqrt{\rho} r'(\rho) \geq \varepsilon$ for all $\rho \geq \rho_0$, which implies

$$\int_0^\infty r'(\rho) d\rho \geq \varepsilon \int_{\rho_0}^\infty \frac{d\rho}{\sqrt{\rho}} = \infty,$$

a contradiction. Setting $t_k := \sqrt{\rho_k}$ yields $t_k \rightarrow \infty$ and $t_k r'(t_k^2) \rightarrow 0$. Along $u(t_k) = t_k v$ we therefore have $\|\nabla f(u(t_k))\| \rightarrow 0$ while $f(u(t_k)) - f^* \rightarrow 1$. Consequently, no $\mu > 0$ can satisfy a global PL inequality $\|\nabla f(u)\|^2 \geq 2\mu (f(u) - f^*)$ for all $u \in \mathbb{R}^n$. \square

Given the absence of the global PL condition, we provide convergence guarantees for both smooth and nonsmooth regimes.

Proposition 3.5. (Convergence of stochastic gradient descent). *Let $F(\theta) := \mathbb{E}_z[\ell(p(g_\theta(z)))]$ with iterates confined to a compact set $K \subset \mathbb{R}^p$.*

1. **Smooth Regime:** *If \mathbb{P} is absolutely continuous, F is continuously differentiable and L -smooth on K . SGD with step size $\eta_t \propto T^{-1/2}$ satisfies:*

$$\min_{0 \leq t \leq T} \mathbb{E}[\|\nabla F(\theta_t)\|^2] = \mathcal{O}(T^{-1/2}).$$

2. **Nonsmooth Regime:** *For general distributions or non-smooth losses, F is locally Lipschitz. Stochastic Subgradient Descent with diminishing steps $\eta_t \rightarrow 0$ converges asymptotically to the set of Clarke stationary points:*

$$\lim_{T \rightarrow \infty} \mathbb{E} \left[\min_{v \in \partial F(\theta_T)} \|v\| \right] = 0.$$

Proof. We differentiate between the smooth and non-smooth regimes based on the properties of the data distribution and the resulting regularity of the composite objective.

Regime I: Smooth Optimization. Assume the data distribution \mathbb{P} is absolutely continuous. As established in Theorem 2.9, the soft-radial projection p is differentiable almost everywhere. Consequently, the event that a pre-activation $u = g_\theta(z)$ lands exactly on the non-differentiable boundary $\partial\mathcal{C}$ has measure zero.

While the pointwise function $f(u) = \ell(p(u))$ is not globally L -smooth (due to Jacobian discontinuities at $\partial\mathcal{C}$), the *expected* objective $F(\theta)$ becomes smooth due to the smoothing effect of the integration over an absolutely continuous distribution. However, to provide a tractable bound on the gradients, we analyze the smoothness of f on the dense open set $U = \mathbb{R}^n \setminus \partial\mathcal{C}$ where p is twice differentiable. Assume $\nabla\ell$ is L_ℓ -Lipschitz on $p(K)$, and on the smooth pieces $U \cap K$, J_p is L_p -Lipschitz. Define the constants over these smooth regions:

$$G_\ell := \sup_{x \in p(K)} \|\nabla\ell(x)\|, \quad B_p := \sup_{u \in K \setminus \partial\mathcal{C}} \|J_p(u)\|.$$

For any u, u' lying in the same connected component of $U \cap K$, we apply the chain rule $\nabla f(u) = J_p(u)^\top \nabla\ell(p(u))$. We decouple the variations in the Jacobian and the loss gradient by adding and subtracting the cross-term $J_p(u)^\top \nabla\ell(p(u'))$, and applying the triangle inequality:

$$\begin{aligned} \|\nabla f(u) - \nabla f(u')\| &= \|J_p(u)^\top \nabla\ell(p(u)) - J_p(u')^\top \nabla\ell(p(u'))\| \\ &= \|J_p(u)^\top \nabla\ell(p(u)) - J_p(u)^\top \nabla\ell(p(u')) + J_p(u)^\top \nabla\ell(p(u')) - J_p(u')^\top \nabla\ell(p(u'))\| \\ &\leq \|J_p(u)\| \|\nabla\ell(p(u)) - \nabla\ell(p(u'))\| + \|\nabla\ell(p(u'))\| \|J_p(u) - J_p(u')\| \\ &\leq B_p L_\ell \|p(u) - p(u')\| + G_\ell L_p \|u - u'\| \\ &\leq (B_p^2 L_\ell + G_\ell L_p) \|u - u'\|. \end{aligned}$$

Thus, f is L -smooth *almost everywhere* with constant $L \leq L_\ell B_p^2 + G_\ell L_p$. Under the assumption of absolute continuity of \mathbb{P} , the objective $F(\theta) = \mathbb{E}[f(g_\theta(z))]$ inherits differentiability, and the variance

of the gradients is bounded by the Lipschitz continuity of f . Applying standard Stochastic Gradient Descent (SGD) with step size $\eta_t \propto 1/\sqrt{T}$ guarantees convergence to a stationary point of F Ghadimi & Lan (2013):

$$\min_{0 \leq t < T} \mathbb{E}[\|\nabla F(\theta_t)\|^2] = \mathcal{O}\left(\frac{1}{\sqrt{T}}\right).$$

Regime II: Nonsmooth Optimization. If the data distribution is discrete or arbitrary, the differentiability of $F(\theta)$ cannot be guaranteed. However, we can establish convergence by relying on the theory of *tame functions* Davis et al. (2020). This framework covers the vast majority of deep learning architectures and ensures that stochastic subgradient methods converge effectively, provided the objective satisfies two structural properties:

1. **Lipschitz Continuity:** As a consequence of Lemma 2.3, the soft-radial projection p is locally Lipschitz. Since the loss ℓ and the network g_θ (e.g., with ReLU activations) are also locally Lipschitz, their composition $F(\theta)$ inherits this property. This guarantees that the Clarke subdifferential $\partial F(\theta)$ is non-empty and uniformly bounded on compact sets.
2. **Tame Objective:** The convergence results of Davis et al. (2020) apply to the class of *tame* functions. This class encompasses functions constructed from finite compositions of piecewise-polynomials and algebraic operations. Since standard activations (like ReLU) are piecewise-polynomial, and our soft-radial projection is constructed from norms and algebraic radial mappings (assuming a semi-algebraic constraint set \mathcal{C} , such as a polytope or ball), the composite objective satisfies this property. This guarantees that the loss landscape is geometrically well-behaved, preventing pathological infinite oscillations.

Davis et al. (2020, Thm. 3.2) proved that for any locally Lipschitz, tame function, the Stochastic Subgradient Method with diminishing step sizes $\eta_t \rightarrow 0$ (and $\sum \eta_t = \infty$, $\sum \eta_t^2 < \infty$) converges almost surely to the set of Clarke stationary points:

$$\lim_{T \rightarrow \infty} \mathbb{E} \left[\min_{v \in \partial F(\theta_T)} \|v\| \right] = 0.$$

This result holds even if the iterates traverse the non-differentiable boundary $\partial\mathcal{C}$, provided the standard bounded variance assumption on the subgradients is met. In our case, this is guaranteed by the local Lipschitz property of the objective on the compact set K . \square

B.3 Proofs of Section 4

Finally, we prove that the constrained model inherits the universal approximation capabilities of the underlying unconstrained architecture.

Theorem 4.1. (Universal approximation on \mathcal{C}). *Let $\mathcal{Z} \subset \mathbb{R}^d$ be compact and let \mathcal{G} be a universal approximator on \mathcal{Z} . For every continuous function $h : \mathcal{Z} \rightarrow \mathcal{C}$ and every $\varepsilon > 0$, there exists a function $g \in \mathcal{G}$ such that the constrained predictor $p \circ g$ satisfies*

$$\sup_{z \in \mathcal{Z}} \|p(g(z)) - h(z)\| \leq \varepsilon.$$

Proof. Without loss of generality, we assume $0 \in \text{Int}(\mathcal{C})$ serves as the anchor point (see Coordinate Convention in Section 2). Throughout this proof, we denote the uniform norm of a function $\psi : \mathcal{Z} \rightarrow \mathbb{R}^n$ by $\|\psi\|_\infty := \sup_{z \in \mathcal{Z}} \|\psi(z)\|$. We separate the interior and boundary cases.

Interior case. Assume the target image satisfies $h(\mathcal{Z}) \subset \text{Int}(\mathcal{C})$. Since $p : \mathbb{R}^n \rightarrow \text{Int}(\mathcal{C})$ is a homeomorphism (Theorem 2.8), the function $\phi := p^{-1} \circ h : \mathcal{Z} \rightarrow \mathbb{R}^n$ is continuous. Since \mathcal{Z} is compact, the image $\phi(\mathcal{Z})$ is compact. Fix any $\delta_0 > 0$ (e.g., $\delta_0 = 1$) and define the compact δ_0 -thickening

$$K := \{\xi \in \mathbb{R}^n \mid \text{dist}(\xi, \phi(\mathcal{Z})) \leq \delta_0\},$$

where $\text{dist}(\xi, A) := \inf_{a \in A} \|\xi - a\|$. By the local Lipschitz continuity of p on the compact set K , there exists a constant $L_K < \infty$ such that $\|p(a) - p(b)\| \leq L_K \|a - b\|$ for all $a, b \in K$. By the universality of \mathcal{G} , there exists a function $g \in \mathcal{G}$ such that

$$\|g - \phi\|_\infty \leq \delta, \quad \delta := \min\left\{\delta_0, \frac{\varepsilon}{L_K}\right\}.$$

This implies $g(\mathcal{Z}) \subset K$. Consequently, for all $z \in \mathcal{Z}$:

$$\begin{aligned} \|p(g(z)) - h(z)\| &= \|p(g(z)) - p(\phi(z))\| \\ &\leq L_K \|g(z) - \phi(z)\| \\ &\leq L_K \delta \leq \varepsilon, \end{aligned}$$

which implies $\|p \circ g - h\|_\infty \leq \varepsilon$, proving the claim for the interior case.

Boundary case. For a general target $h : \mathcal{Z} \rightarrow \mathcal{C}$, we define a strictly interior approximation h_ε by shrinking h towards the anchor. Define the shrink operator $S_\tau(x) := (1 - \tau)x$. Since \mathcal{C} is convex and $0 \in \text{Int}(\mathcal{C})$, we have $S_\tau(\mathcal{C}) \subset \text{Int}(\mathcal{C})$ for any $\tau \in (0, 1)$. Let $D := \|h\|_\infty < \infty$. If $D = 0$, then $h \equiv 0$, and the interior case applies directly. Otherwise, we select a shrinkage factor τ sufficiently small to ensure h_ε remains within $\varepsilon/2$ of h . Specifically, set:

$$\tau := \min\left\{\frac{1}{2}, \frac{\varepsilon}{2D}\right\} \in (0, 1), \quad h_\varepsilon := S_\tau \circ h.$$

The uniform distance between the original and shrunken target is bounded by

$$\|h_\varepsilon - h\|_\infty = \sup_{z \in \mathcal{Z}} \|(1 - \tau)h(z) - h(z)\| = \tau D \leq \frac{\varepsilon}{2}.$$

Since the new target satisfies $h_\varepsilon(\mathcal{Z}) \subset \text{Int}(\mathcal{C})$, we can invoke the *Interior case* result with precision $\varepsilon/2$. This guarantees the existence of a function $g \in \mathcal{G}$ such that

$$\|p \circ g - h_\varepsilon\|_\infty \leq \frac{\varepsilon}{2}.$$

Finally, applying the triangle inequality yields the total error bound

$$\|p \circ g - h\|_\infty \leq \underbrace{\|p \circ g - h_\varepsilon\|_\infty}_{\leq \varepsilon/2} + \underbrace{\|h_\varepsilon - h\|_\infty}_{\leq \varepsilon/2} \leq \varepsilon.$$

□

C Extended Numerical Results

In this section, we first provide additional insights into the model parameters, specifically how the radial contraction function $r(\cdot)$ and the scale parameter λ influence the effective optimization landscape. Next, we provide implementation details for the competitor algorithms, DC3 (Donti et al., 2021) and HardNet (Min & Azizan, 2024), which were adjusted to accommodate the (capped) simplex constraints considered in our experiments. We then detail the architectures and hyperparameters utilized within our study. Finally, we conclude with a comprehensive description of our experimental setups.

C.1 Sensitivity Analysis: Radial Contraction and Scaling

In Sec. 5.1 we introduced radial contraction functions $r(\cdot)$ satisfying the properties of Assumption 2.4. The *rational* radial contraction decays polynomially ($\mathcal{O}(\rho^{-1})$), whereas the *exponential* and *hyperbolic* forms exhibit exponential decay. Consequently, the rational link preserves larger gradient magnitudes for predictions falling far outside the feasible set ($\rho \gg 1$), which helps mitigate the vanishing gradient problem for extreme outliers.

Similar to the problem illustrated in Fig. 1, we evaluate the role of $r(\cdot)$ in terms of warping the effective loss landscape (A), influencing the training loss (B), and determining the convergence to the target x^* . Figures 3, 4, and 5 visualize the effective loss landscape for the *rational* (3), *exponential* (4), and *hyperbolic* (5) functions, respectively. Furthermore, we illustrate in Fig. 6 how the minimum scaling threshold ε modifies the landscape geometry surrounding the chosen anchor u_0 .

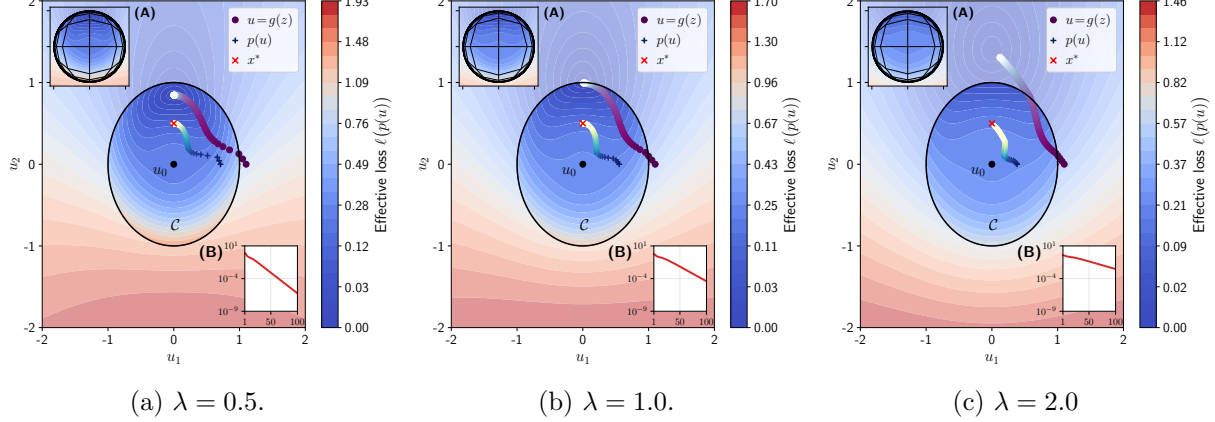


Figure 3: Soft-radial projection $p(u)$ with *rational* radial contraction (3).

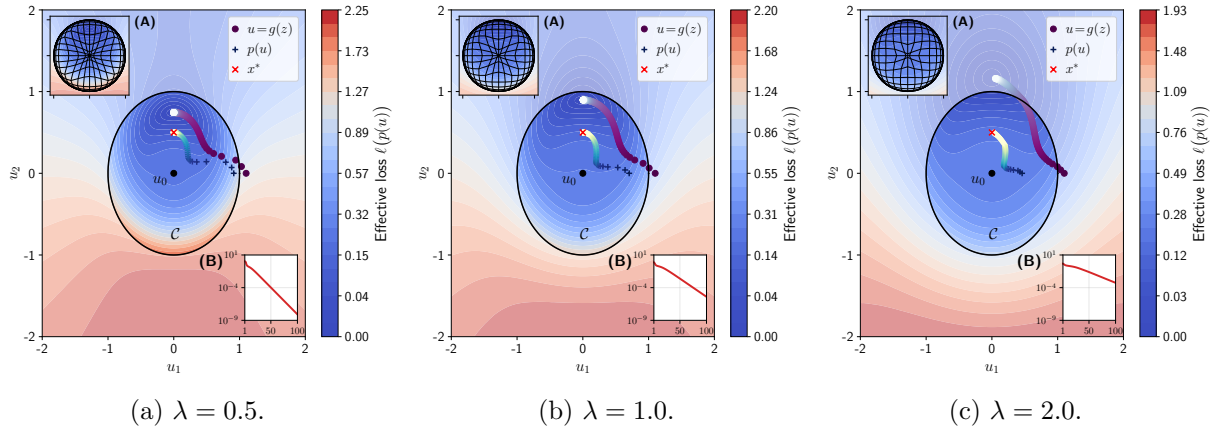


Figure 4: Soft-radial projection $p(u)$ with *exponential* radial contraction (4).

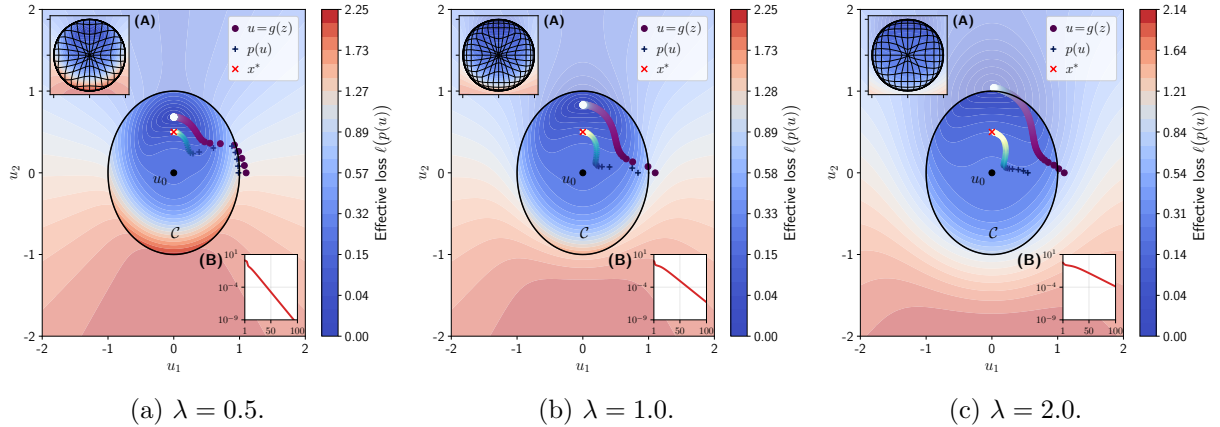


Figure 5: Soft-radial projection $p(u)$ with *hyperbolic* radial contraction (5).

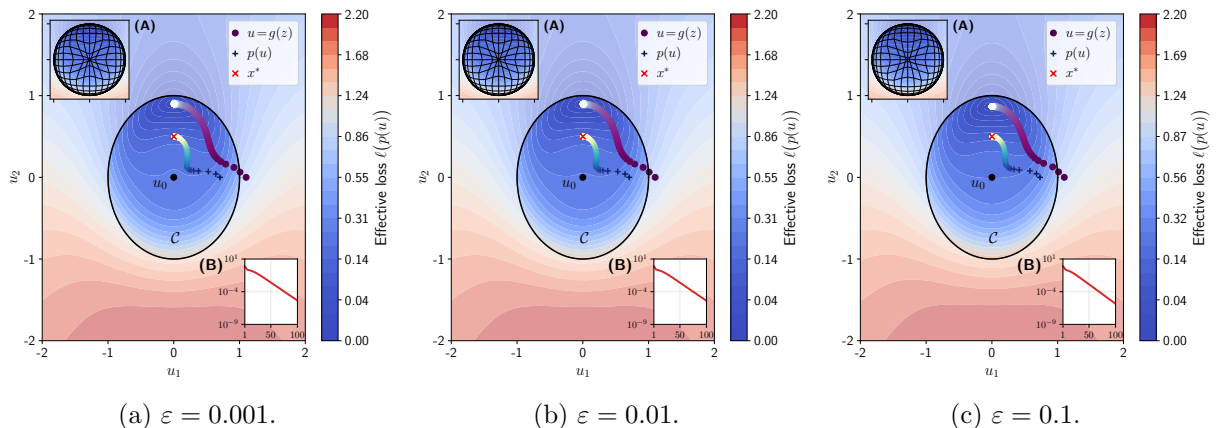


Figure 6: Soft-radial projection $p(u)$ for varying minimum scaling threshold ε .

C.2 Adaptation of Competitor Methods to Capped Simplex Constraints

We explain the adaptation of the competitor methods with respect to the capped simplex introduced in the portfolio setting and formally defined as

$$\mathcal{C} = \left\{ w \in \mathbb{R}^N \mid 0 \leq w, \mathbf{1}^\top w = 1, w \leq c \right\},$$

where w is the portfolio weight and c is a cap on the weight.

HardNet. The HardNet framework Min & Azizan (2024) enforces feasibility by appending a differentiable projection layer to an unconstrained predictor $g_\theta : \mathcal{Z} \rightarrow \mathbb{R}^N$. Given an input $z \in \mathcal{Z}$ and raw output $u := g_\theta(z)$, the method considers input-dependent affine constraints of the form

$$\underline{b}(z) \leq A(z)w \leq \bar{b}(z).$$

Min & Azizan (2024) derive a closed-form projection for this case, denoted *HardNet-Aff*:

$$P_{\text{HN}}(u; z) = u + A_R^\dagger(z) \left(\text{ReLU}(\underline{b}(z) - A(z)u) - \text{ReLU}(A(z)u - \bar{b}(z)) \right), \quad (10)$$

where $A_R^\dagger(z) := A(z)^\top (A(z)A(z)^\top)^{-1}$ is the Moore–Penrose *right* pseudoinverse. This closed form assumes that $A(z)$ has full row rank (Assumption 5 in Min & Azizan (2024)), describing an underdetermined system. In our portfolio setting, the feasible set is a capped simplex; stacking the equality constraint with the $2N$ bound constraints yields an *overdetermined* affine system. Consequently, the matrix AA^\top is singular and the right-pseudoinverse expression in (10) is not directly applicable. We therefore use a least-squares relaxation of the HardNet correction. This involves defining a (signed) violation vector

$$v(u; z) := \text{ReLU}(\underline{b}(z) - Au) - \text{ReLU}(Au - \bar{b}(z)). \quad (11)$$

Since the resulting static constraint matrix A has full column rank in our construction, we compute a least-squares correction direction via the *left* pseudoinverse

$$\Delta(u; z) := \arg \min_{\Delta \in \mathbb{R}^N} \|A\Delta - v(u; z)\|^2 = A_L^\dagger v(u; z), \quad A_L^\dagger := (A^\top A)^{-1} A^\top. \quad (12)$$

We then set $\tilde{w} := u + \Delta(u; z)$. A conceptually broader but computationally slower alternative proposed by the authors for general convex constraints is to embed the projection as a differentiable convex optimization layer Agrawal et al. (2019), referred to as *HardNet-Cvx*. To remove any remaining numerical residuals during evaluation, we additionally apply an exact orthogonal projection onto the capped simplex, $w = P(\tilde{w})$, to guarantee $w \in \mathcal{C}$.

Symmetric DC3 for the capped simplex. We adapt the Deep Constraint Completion and Correction (DC3) framework (Donti et al., 2021) to \mathcal{C} . Standard DC3 selects $N - 1$ independent variables and defines the remaining coordinate as dependent via the equality constraint. Applied directly to the raw network output $u = g_\theta(z)$, this introduces an asymmetry: the dependent coordinate absorbs the entire sum deviation, often producing unstable magnitudes and gradients. To mitigate this, we employ a *symmetric* initialization that first distributes the sum deviation evenly

by orthogonally projecting u onto the simplex hyperplane $\mathcal{H} := \{w \in \mathbb{R}^N : \mathbf{1}^\top w = 1\}$. Concretely, we set

$$w^{(0)} := P_{\mathcal{H}}(u) = u - \frac{1}{N}(\mathbf{1}^\top u - 1)\mathbf{1} \in \mathcal{H}. \quad (13)$$

We then take the first $N - 1$ coordinates as free variables $\xi := (w_1^{(0)}, \dots, w_{N-1}^{(0)})^\top \in \mathbb{R}^{N-1}$ and enforce the equality constraint through a completion map

$$w(\xi) := \begin{bmatrix} \xi \\ 1 - \mathbf{1}^\top \xi \end{bmatrix}, \quad (14)$$

which ensures $\mathbf{1}^\top w(\xi) = 1$ for all ξ . To correct violations of the bound constraints $0 \leq w \leq c$, we minimize a squared hinge-residual energy

$$\mathcal{V}(\xi) := \sum_{i=1}^N \left(\text{ReLU}(-w_i(\xi))^2 + \text{ReLU}(w_i(\xi) - c_i)^2 \right), \quad (15)$$

via an unrolled gradient descent loop on the free variables

$$\xi^{(t+1)} = \xi^{(t)} - \eta \nabla_{\xi} \mathcal{V}(\xi^{(t)}), \quad t = 0, \dots, L-1. \quad (16)$$

The final output is given by $w^{(L)} = w(\xi^{(L)})$. Gradients are backpropagated through the completion map (14), properly accounting for the dependence of the dependent coordinate on the free variables. Similar to the HardNet implementation, we apply an orthogonal projection during evaluation to ensure strict feasibility.

C.3 Hyperparameter Tuning

Table 4 summarizes the hyperparameters used in our experiments, distinguishing between the portfolio optimization and ride-sharing dispatch task. For both domains, we perform a grid search to select the optimal configuration based on validation performance. As noted earlier, for HardNet and DC3, we apply a final orthogonal projection to the candidate solution during evaluation only. This ensures that the evaluation metrics are not penalized by minor infeasibilities caused by numerical rounding errors. Crucially, we omit this strict projection step during training to preserve gradient flow and prevent the deterioration of learning signals.

C.4 Extended Analysis: Portfolio Optimization

C.4.1 Discussion: Deep Portfolio Optimization vs. Classical Approaches

The formulation presented in Section 5.2 represents a *deep portfolio optimization* problem Zhang et al. (2020), which fundamentally differs from the classical mean-variance optimization framework Markowitz (1952).

Predict-then-Optimize vs. End-to-End Learning. Classical mean-variance optimization typically operates in a “predict-then-optimize” framework: one first estimates the expected return vector $\mu \in \mathbb{R}^N$ and the covariance matrix $\Sigma \in \mathbb{S}_+^N$, and then solves a quadratic program to maximize $w^\top \mu - \zeta w^\top \Sigma w$. This two-step process suffers from two major limitations. First, it

Table 4: Hyperparameter settings for portfolio optimization and ride-sharing dispatch experiments.

Parameter	Portfolio Optimization	Ride-Sharing Dispatch
<i>Architecture & Training</i>		
Base Architecture	LSTM	MLP
Hidden Units	$\{32, 64\}$	
Dropout Rate	$\{0.1, 0.2\}$	
Optimizer	Adam	
Learning Rate	$\{1 \times 10^{-4}, 5 \times 10^{-4}\}$	
Lookback Horizon (H)	$\{10, 30\}$	24
Batch Size	64	128
Training Epochs	50	100
<i>Projection Layer Hyperparameters</i>		
Softmax Temperature (τ)	$\{0.1, 0.5, 1.0, 2.0\}$	
Soft-radial λ	$\{0.5, 1.0, 2.0, 5.0, 10.0\}$	
Soft-radial $r(\cdot)$	$\{\text{Fractional, Exponential, Hyperbolic}\}$	
HardNet Steps	$\{1, 3, 5\}$	
DC3 Steps	$\{1, 3, 5\}$	
DC3 Learning Rate	$\{10^{-2}, 10^{-1}\}$	
DC3 Momentum	$\{0.5, 0.9\}$	

separates the prediction error from the optimization cost; a small error in estimating Σ can lead to drastically suboptimal portfolios (a phenomenon formally known as the “error maximization” property of Markowitz Michaud (1989)). Second, while standard sample estimators neglect temporal dependencies (implicitly assuming i.i.d. returns), more advanced dynamic estimators (*e.g.*, generalized autoregressive conditional heteroskedasticity (GARCH) model) often impose rigid parametric structures that fail to capture the complex, non-linear interactions between assets that recurrent neural network architectures in the form of g_θ are designed to exploit.

Parameter Sensitivity and Convexity. A significant hurdle in classical frameworks is the sensitivity to the risk-aversion parameter ζ , which requires frequent recalibration. Our formulation bypasses this by directly maximizing the Sharpe ratio—a scale-invariant metric that eliminates the need for a subjective risk-return trade-off coefficient. While the static Sharpe ratio maximization is a quasiconcave problem that can be reformulated as a Second-Order Cone Program (SOCP) for global convergence, parameterizing the weights via a neural network g_θ introduces non-convexity. We accept this trade-off to leverage the representational power of deep learning; the model can ingest complex state histories to generate non-linear weight mappings, far surpassing the constraints of the linear-quadratic assumptions in traditional finance.

Transaction Cost as Temporal Regularization. Finally, we address the cost of trading. Classical frameworks often use static L_2 regularization to prevent overfitting or L_1 regularization to enforce sparsity Brodie et al. (2009). However, these spatial constraints fail to penalize policy volatility: a network can satisfy strict sparsity constraints while still oscillating wildly between assets over time.

To enforce temporal consistency, we explicitly model transaction costs via the term $\frac{\gamma}{2} \|w_t - w_{t-1}^+\|_1$. Unlike static penalties, this targets the velocity of the portfolio turnover. Crucially, costs are computed relative to the *drifted* portfolio w_{t-1}^+ , ensuring that passive price movements do not incur

penalties. Let w_{t-1} be the weights at $t-1$. Over the interval $(t-1, t]$, price movements y_t cause these weights to evolve naturally into the drifted weights $w_{t-1}^+ = (\text{diag}(y_t) w_{t-1}) / (y_t^\top w_{t-1})$. The numerator captures asset-specific growth, while the denominator renormalizes the sum.

Remark C.1 (Cost normalization). The factor $1/2$ normalizes the L_1 distance to represent *one-way turnover* (the fraction of portfolio value actively replaced). Thus, γ represents the effective cost per unit of turnover.

This formulation has a profound effect on the learning dynamics. By including this cost directly in the objective, the gradient signal penalizes high-frequency control noise. The policy learns a valid economic trade-off: it naturally creates a *hysteresis effect*, where the portfolio weights exhibit inertia against small market fluctuations. This recovers the classical *no-trade zone* behavior predicted by Davis & Norman (1990): rebalancing is only performed if the expected Sharpe ratio gain strictly outweighs the explicit cost of the action.

C.4.2 Descriptive Statistics

In Table 5, we provide descriptive statistics for the asset universes included in our analysis. We evaluate performance across three distinct portfolios, each representing a different difficulty level and correlation structure:

- *Global*: The Global portfolio aggregates a diverse set of multi-asset class indices covering global equities, treasury bonds, and commodities. It represents a macro-allocation problem characterized by lower average correlation.
- *Sectors*: The Sectors dataset comprises the 11 primary Global Industry Classification Standard (GICS) sectors. It serves as a standard industry benchmark with high inter-asset correlation, effectively representing the broader US economy.
- *Liquid*: The Liquid collection contains a selection of 50 high-volume individual stocks. This universe captures the higher volatility and idiosyncratic risk associated with individual stock picking.

Returns are derived from Yahoo Finance adjusted closing prices to account for corporate actions, such as splits and dividends, and are partitioned chronologically to strictly prevent look-ahead bias.³ The training set spans from 2010/01/01 to 2018/12/31, covering the post-financial-crisis recovery. The validation set, used for hyperparameter tuning, covers 2019/01/01 to 2020/12/31. The test set extends from 2021/01/01 to 2025/12/31.

Table 5 reports the annualized mean and median returns alongside annualized volatility. To fully characterize the risk profile and market dynamics, we also include the Maximum Drawdown (Max DD), the average pairwise correlation between assets ($\bar{\rho}$), the lag-1 autocorrelation (AC(1)), and the Kolmogorov-Smirnov p -value (p_{KS}). As shown in the table, the test period exhibits significantly higher volatility and maximum drawdown compared to the training period, reflecting more turbulent market conditions. This distribution shift is quantified by p_{KS} : for the Global, Liquid, and Sectors universes, $p_{KS} < 0.05$ in the test set, rejecting the null hypothesis that the test data follows the training distribution. This confirms that our evaluation effectively tests the model’s generalization to out-of-distribution market regimes.

³We note that survivorship bias is not compensated for within our analysis, and assets with missing data are omitted from the study.

Table 5: Summary statistics. Returns, Volatility, and Drawdown are in percentages. $\bar{\rho}$ is average correlation. p_{KS} tests for regime shift.

Universe	Split	μ (%)	Median (%)	σ (%)	MaxDD (%)	$\bar{\rho}$	AC(1)	p_{KS}
Global	Train	7.30	11.84	17.47	-19.37	0.35	-0.037	
Global	Val	7.46	14.22	15.68	-13.87	0.32	-0.020	0.607
Global	Test	9.30	13.60	22.34	-28.46	0.46	-0.045	0.011
Liquid	Train	19.12	14.72	24.98	-16.11	0.38	-0.021	
Liquid	Val	19.71	30.76	25.40	-18.11	0.39	-0.029	0.319
Liquid	Test	16.95	16.93	31.44	-30.56	0.40	-0.088	0.019
Sectors	Train	13.46	20.17	17.05	-18.61	0.70	-0.037	
Sectors	Val	9.75	26.72	17.15	-18.47	0.58	-0.003	0.826
Sectors	Test	13.99	22.01	24.57	-36.91	0.65	-0.107	0.007

C.4.3 Implementation Details

In the portfolio optimization setting, we augment raw asset returns with rolling volatility and rolling correlation to a cross-sectional market proxy (defined as the mean return across the universe). These features are computed over the lookback horizon H and normalized using training-set statistics to strictly prevent look-ahead bias. We acknowledge that achieving state-of-the-art financial performance typically requires a broader set of predictive signals (alphas). However, our primary objective is to evaluate the stability of the learning process under the high noise-to-signal ratio characteristic of financial time series, rather than to maximize the Sharpe ratio through signal engineering.

As discussed in Sec. 5.2, the L_1 transaction cost term in (7) is non-differentiable at zero, posing a challenge for gradient-based optimization. To address this, we replace the exact L_1 -norm with the Pseudo-Huber loss, a reparameterization of the smooth penalty introduced by Charbonnier et al. (1994), defined as

$$L_\delta(w_t, w_{t-1}^+) = \sum_{i=1}^N \left(\sqrt{\delta^2 + (w_{i,t} - w_{i,t-1}^+)^2} - \delta \right) \quad (17)$$

where $\delta > 0$ controls the steepness. As $\delta \rightarrow 0$, this function converges to $\|w_t - w_{t-1}^+\|_1$, preserving theoretical consistency while enabling stable gradient flow.

C.4.4 Additional Empirical Results

In Section 5, we presented results for the Sharpe ratio maximization formulation defined in (7). A common concern in practice is that the explicit inclusion of transaction costs may encourage trivial solutions where the network prioritizes weight stability over active performance optimization. To address this, we provide comparative results for portfolio optimization where training is performed without modeling transaction costs (i.e., omitting the $\frac{\gamma}{2} \|w_t - w_{t-1}^+\|_1$ term). We refer to the formulation excluding these costs from the loss function as *training gross*, and the standard formulation including them as *training net*. Crucially, to ensure a fair comparison, we report the net Sharpe ratio and turnover for both configurations during evaluation. Table 6 and Table 7 present the

aggregated results for the *training gross* and *training net* settings, respectively. Overall, we observe that explicitly considering transaction costs during training leads to a decrease in test-time turnover across methods. Consistent with our findings in Section 5, our *soft-radial projection* demonstrates superior financial performance and greater robustness to random seed initialization.

Table 6: Portfolio optimization results for the *training gross* objective (costs omitted from loss), aggregated over five random seeds (mean \pm std).

Universe	Feasible Set	Method	Sharpe Ratio (Net)	Turnover
Global	Δ	Softmax	0.03 (± 0.29)	0.27 (± 0.04)
		O-Proj	0.15 (± 0.32)	0.23 (± 0.05)
		Soft-Radial	0.55 (± 0.04)	0.06 (± 0.02)
Global	$c = 0.15$	O-Proj	0.33 (± 0.13)	0.15 (± 0.01)
		DC3	0.34 (± 0.14)	0.19 (± 0.01)
		HardNet	0.43 (± 0.13)	0.17 (± 0.02)
		Soft-Radial	0.60 (± 0.09)	0.06 (± 0.02)
Liquid	Δ	Softmax	0.61 (± 0.32)	0.22 (± 0.05)
		O-Proj	0.44 (± 0.25)	0.44 (± 0.02)
		Soft-Radial	0.87 (± 0.03)	0.09 (± 0.01)
Liquid	$c = 0.05$	O-Proj	0.56 (± 0.12)	0.20 (± 0.01)
		DC3	0.49 (± 0.18)	0.23 (± 0.02)
		HardNet	0.59 (± 0.19)	0.20 (± 0.01)
		Soft-Radial	0.87 (± 0.02)	0.07 (± 0.01)
Sectors	Δ	Softmax	0.39 (± 0.16)	0.26 (± 0.04)
		O-Proj	0.56 (± 0.14)	0.23 (± 0.02)
		Soft-Radial	0.74 (± 0.04)	0.11 (± 0.02)
Sectors	$c = 0.5$	O-Proj	0.58 (± 0.08)	0.21 (± 0.03)
		DC3	0.55 (± 0.07)	0.20 (± 0.02)
		HardNet	0.63 (± 0.07)	0.20 (± 0.03)
		Soft-Radial	0.75 (± 0.05)	0.13 (± 0.02)
Sectors	$c = 0.15$	O-Proj	0.73 (± 0.10)	0.09 (± 0.00)
		DC3	0.72 (± 0.02)	0.07 (± 0.00)
		HardNet	0.82 (± 0.05)	0.07 (± 0.01)
		Soft-Radial	0.82 (± 0.03)	0.03 (± 0.01)

Table 7: Portfolio optimization results for the *training net* objective (costs included in loss), aggregated over five random seeds (mean \pm std).

Universe	Feasible Set	Method	Sharpe Ratio (Net)	Turnover
Global	Δ	Softmax	0.21 (± 0.29)	0.31 (± 0.04)
		O-Proj	0.27 (± 0.20)	0.20 (± 0.03)
		Soft-Radial	0.68 (± 0.09)	0.05 (± 0.03)
Global	$c = 0.15$	O-Proj	0.49 (± 0.18)	0.17 (± 0.02)
		DC3	0.38 (± 0.15)	0.18 (± 0.02)
		HardNet	0.44 (± 0.13)	0.16 (± 0.02)
Liquid	Δ	Soft-Radial	0.68 (± 0.05)	0.05 (± 0.01)
		Softmax	0.63 (± 0.19)	0.22 (± 0.05)
		O-Proj	0.25 (± 0.18)	0.48 (± 0.02)
Liquid	$c = 0.05$	Soft-Radial	0.90 (± 0.03)	0.06 (± 0.00)
		O-Proj	0.64 (± 0.09)	0.22 (± 0.01)
		DC3	0.63 (± 0.08)	0.23 (± 0.01)
Sectors	Δ	HardNet	0.62 (± 0.11)	0.19 (± 0.01)
		Soft-Radial	0.90 (± 0.02)	0.05 (± 0.00)
		Softmax	0.43 (± 0.24)	0.25 (± 0.04)
Sectors	$c = 0.5$	O-Proj	0.68 (± 0.21)	0.21 (± 0.03)
		DC3	0.76 (± 0.04)	0.09 (± 0.03)
		HardNet	0.73 (± 0.23)	0.18 (± 0.02)
Sectors	$c = 0.15$	Soft-Radial	0.72 (± 0.08)	0.17 (± 0.02)
		O-Proj	0.66 (± 0.08)	0.19 (± 0.03)
		DC3	0.77 (± 0.07)	0.12 (± 0.02)
Sectors	$c = 0.15$	HardNet	0.80 (± 0.06)	0.09 (± 0.01)
		Soft-Radial	0.78 (± 0.06)	0.07 (± 0.00)
		O-Proj	0.84 (± 0.02)	0.06 (± 0.01)
		DC3	0.87 (± 0.04)	0.02 (± 0.00)

C.5 Extended Analysis: Ride-Sharing Dispatch

Our taxi dataset is derived from the publicly available records of the NYC Taxi and Limousine Commission (TLC) for the period of January to June 2024. To ensure a robust evaluation of temporal generalization, the data is split chronologically into 70% training, 15% validation, and 15% testing sets. To capture the multi-scale periodicity of urban mobility, we represent temporal states using cyclical sine-cosine encodings for both daily and weekly cycles. Unlike categorical indicators that create artificial boundaries at midnight, this continuous representation allows the policy network g_θ to learn smooth, time-dependent transition boundaries. This enables the model to proactively align fleet distribution with anticipated demand peaks, maximizing the global served rate within the constraints of the time-varying supply S_t .

In Section 5 (Table 2), we presented results for an MLP model subject to the scaled capped simplex with $\kappa = 0.1$. Here, we introduce a more challenging experimental setting with $\kappa = 0.02$. This tighter constraint creates a significantly more difficult allocation problem, requiring the distribution of the fleet across all $N = 150$ zones with strictly limited per-zone capacity. For completeness,

we also provide results for projection onto the standard simplex. While this baseline serves as a reference point consistent with Table 2, we observe a clear deterioration in performance for the constrained models under this stricter regime, characterized by a lower volume of served customers (*cf.* Table 8). Consistent with the less constrained objective, most methods perform equivalently, with the notable exception of the orthogonal projection. These findings suggest that across the set of projection methods, performance is heavily influenced by data noise and model complexity.

Table 8: Ride sharing dispatch results aggregated over five random seeds (mean \pm std).

Feasible Set	Method	Served Rate
Δ	Softmax	0.83 (± 0.00)
$\kappa = 0.02$	O-Proj	0.64 (± 0.00)
	DC3	0.69 (± 0.00)
	HardNet	0.69 (± 0.00)
	Soft-Radial	0.69 (± 0.00)